pubs.acs.org/acschemicalbiology

Articles

Radiation-Induced Lipid Peroxidation Triggers Ferroptosis and Synergizes with Ferroptosis Inducers

Ling F. Ye, Kunal R. Chaudhary, Fereshteh Zandkarimi, Andrew D. Harken, Connor J. Kinslow, Pavan S. Upadhyayula, Athanassios Dovas, Dominique M. Higgins, Hui Tan, Yan Zhang, Manuela Buonanno, Tony J. C. Wang, Tom K. Hei, Jeffrey N. Bruce, Peter D. Canoll, Simon K. Cheng,* and Brent R. Stockwell*,

Cite This: https://dx.doi.org/10.1021/acschembio.9b00939

Read Online

ACCESS | Metrics & More | Article Recommendations | Supporting Information

ABSTRACT: Although radiation is widely used to treat cancers, resistance mechanisms often develop and involve activation of DNA repair and inhibition of apoptosis. Therefore, compounds that sensitize cancer cells to radiation via alternative cell death pathways are valuable. We report here that ferroptosis, a form of nonapoptotic cell death driven by lipid peroxidation, is partly responsible for radiation-induced cancer cell death. Moreover, we found that small molecules activating ferroptosis through system x_c^- inhibition or GPX4 inhibition synergize with radiation to induce ferroptosis in several cancer types by enhancing cytoplasmic lipid peroxidation but not increasing DNA damage or caspase activation. Ferroptosis inducers synergized with cytoplasmic irradiation, but not nuclear irradiation. Finally, administration of ferroptosis inducers enhanced the antitumor effect of radiation in a murine xenograft model and in human patient-derived models of lung adenocarcinoma and glioma. These results suggest that ferroptosis inducers may be effective radiosensitizers that can expand the efficacy and range of indications for radiation therapy.

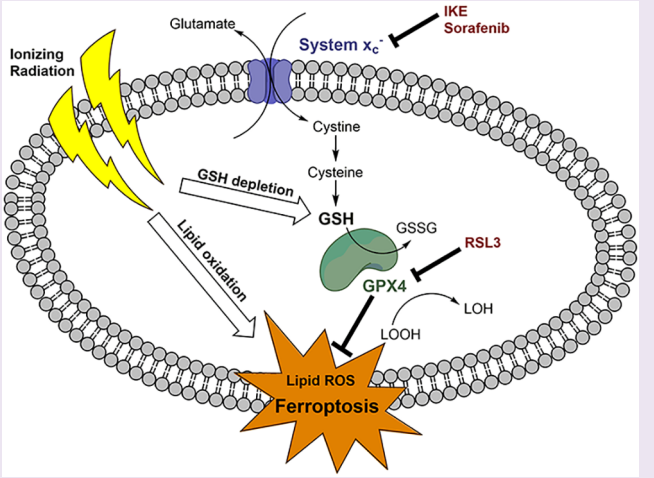

Radiation therapy is one of the most important therapeutic modalities in the treatment of cancer, which provides both curative and palliative strategies for disease management.[1] DNA damage is thought to be the principal target of radiation, and its extent and repair are the most crucial factors determining intrinsic tumor cell death from radiation.[2] While radiation provides targeted local control of malignant lesions, the addition of systemic treatments is often required to provide radiosensitizing effects to tumors, as well as to manage undetected distant disease. To this effect, the combination of chemotherapy and radiation has become more common over the past 30 years.[3] However, tumor control still remains poor with combination chemoradiation therapy in many locally advanced cancers, such as sarcomas, gliomas, and non-small-cell lung cancers, which are historically considered radioresistant.[4,5]

Radiation resistance mechanisms often involve activation of DNA repair pathways and inhibition of apoptosis.[6−8] At the same time, alternative radiation-induced cell death pathways, such as necroptosis and autophagy, have been suggested.[9,10] If activated, these mechanisms might offer strategies for treating otherwise radioresistant tumors.

In addition to DNA damage, radiation also generates reactive oxygen species, which can result in oxidation of biomolecules, such as lipid oxidation.[11] While this effect has largely remained unexplored, a phospholipid-peroxidation-driven form of regulated cell death, ferroptosis, has recently been identified, and increasing evidence has been found to support its importance in a variety of biological and disease processes.[12] Ferroptosis is induced when phospholipid-PUFA peroxidation overwhelms cellular defense systems, such as the capacity of the glutathione phospholipid peroxidase GPX4 and the CoQ_{10}-regenerating enzyme FSP1.[13] Ferroptosis inducers include system x_c^- inhibitors, which prevent cystine uptake into the cell, a building block of glutathione. By decreasing the biosynthesis of glutathione, system x_c^- inhibitors indirectly inhibit the lipid repair function of GPX4, which uses glutathione as a coenzyme. Direct inhibitors of GPX4 can also induce ferroptosis through

Received: November 19, 2019
Accepted: January 3, 2020
Published: January 3, 2020

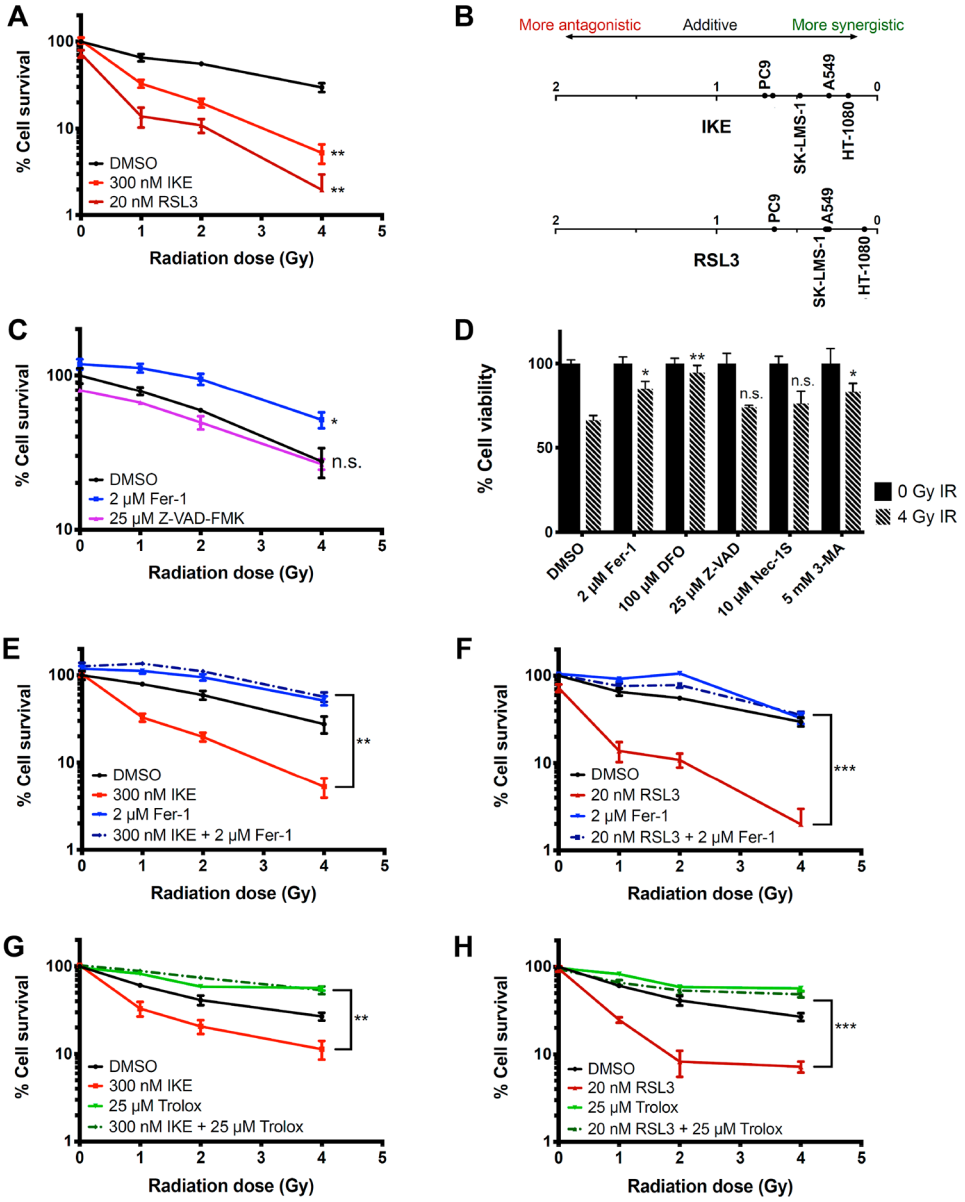

Figure 1. Increase in radiation sensitivity by IKE and RSL3 in cancer cell lines through lipid peroxidation. (A) Dose response of HT-1080 cells treated with DMSO, IKE, or RSL3 to radiation measured by clonogenic assays. $^{**}p < 0.01$. (B) Coefficients of interaction between IKE (top) or RSL3 (bottom) and radiation observed for five tested cancer cell lines measured by clonogenic assays. (C) Dose response of HT-1080 cells treated with DMSO, ferrostatin-1, or Z-VAD-FMK to radiation measured by clonogenic assays. $^{*}p < 0.05$, n.s.: $p > 0.05$. (D) Cell viability of HT-1080 cells treated with DMSO, ferrostatin-1, deferoxamine, Z-VAD-FMK, necrostatin-1S, or 3-methyladenine and cotreated with 0 or 4 Gy radiation for 24 h. Data normalized to 0 Gy unirradiated controls for each treatment group. $^{**}p < 0.01$, $^{*}p < 0.05$, n.s.: $p > 0.05$. (E) Dose response of HT-1080 cells treated with DMSO, IKE, ferrostatin-1, or IKE and ferrostatin-1 measured by clonogenic assays. $^{**}p < 0.01$. Significance is calculated between the group treated with ferroptosis inducer and the group cotreated with ferroptosis inducer and ferroptosis inhibitor in E, F, G, and H. (F) Dose response of HT-1080 cells treated with DMSO, RSL3, ferrostatin-1, or RSL3 and ferrostatin-1 measured by clonogenic assays. $^{***}p < 0.001$. (G) Dose response of HT-1080 cells treated with DMSO, IKE, Trolox, or IKE and Trolox measured by clonogenic assays. $^{**}p < 0.01$. (H) Dose response of HT-1080 cells treated with DMSO, RSL3, Trolox, or RSL3 and Trolox measured by clonogenic assays. $^{***}p < 0.001$. Data are plotted as mean ± SEM; $n = 3$ side-by-side experiments for A, C, D, E, F, G, H. Three biologically independent experiments were performed with similar results.

this mechanism.[14] Numerous cancer cell lines, such as sarcomas, renal cell carcinoma, and diffuse large B-cell lymphomas, have been found to be particularly sensitive to ferroptosis;[14,15] some of these cell lines are also sensitive in the context of xenograft tumor models.[15,16] These data suggest the hypothesis that radiation's antitumor efficacy may in some contexts be driven by triggering ferroptosis and that ferroptosis inducers may be effective radiosensitizers.

RESULTS AND DISCUSSION

IKE and RSL3 Synergize with Radiation to Promote Clonogenic Ferroptotic Cell Death in Cell Lines of Multiple Tumor Types. We sought to determine first whether small molecule inducers of ferroptosis could synergize with radiation to promote cancer cell killing. Toward this end, we treated ferroptosis-sensitive HT-1080 fibrosarcoma cells with different doses of Cs-137 γ radiation and either imidazole ketone erastin (IKE), a system x_c^- inhibitor, or Ras Synthetic Lethal 3

https://dx.doi.org/10.1021/acschembio.9b00939
ACS Chem. Biol. XXXX, XXX, XXX−XXX

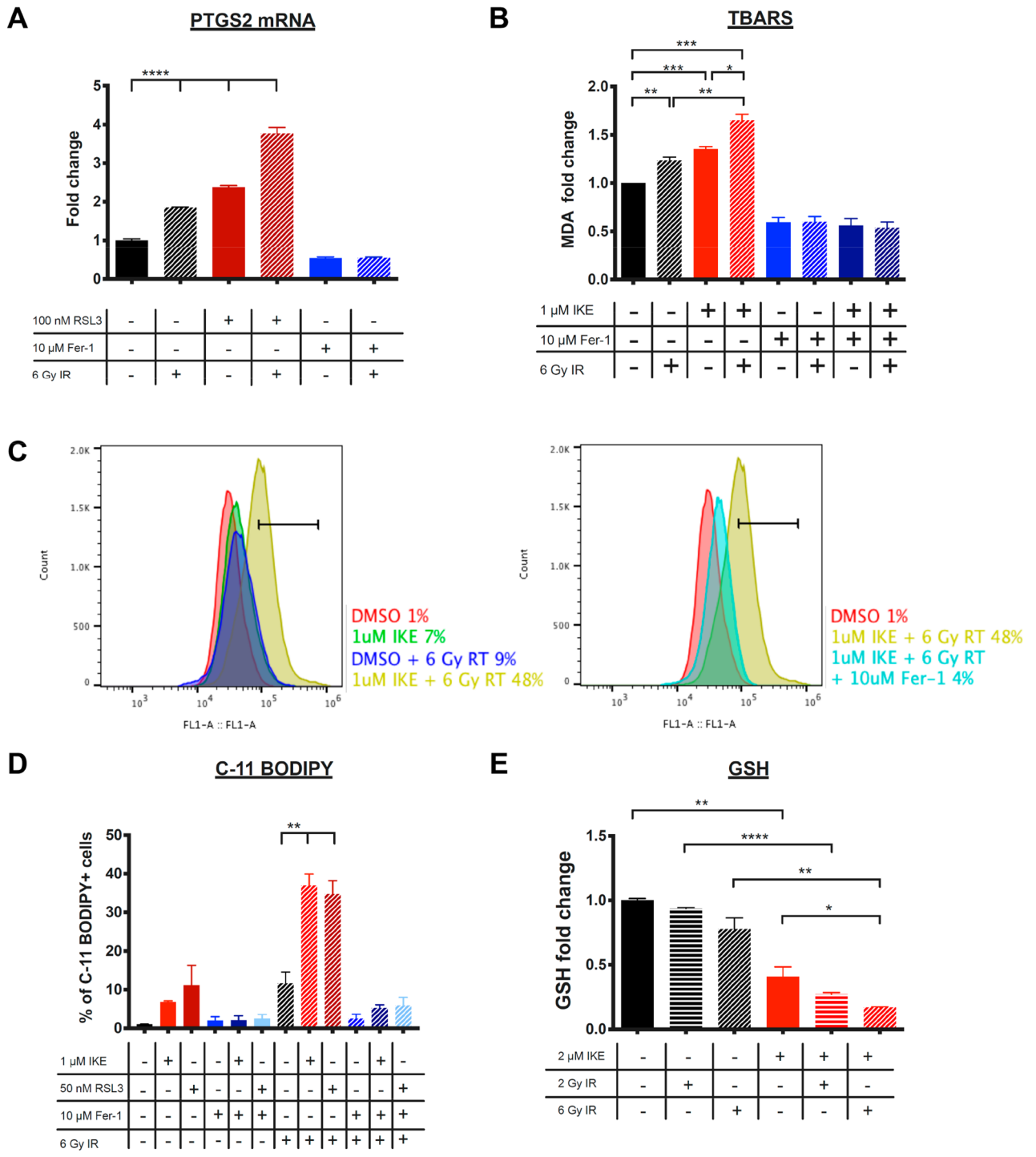

Figure 2. Markers of ferroptosis elevated in HT-1080 cells treated with radiation. (A) PTGS2 mRNA fold change measured by RT-qPCR in HT-1080 cells treated with DMSO, RSL3, or ferrostatin-1 and cotreated with 0 or 6 Gy radiation for 24 h. ****$p < 0.0001$. (B) MDA levels measured using the TBARS assay in HT-1080 cells treated with DMSO, IKE, or ferrostatin-1 and cotreated with 0 or 6 Gy radiation for 24 h. ***$p < 0.001$, **$p < 0.01$, *$p < 0.05$. (C) Representative histograms of HT-1080 cells treated with DMSO, IKE, or IKE + ferrostatin-1 and cotreated with 0 or 6 Gy radiation for 24 h and stained with C-11 BODIPY measured by flow cytometry. Horizontal bars indicate C-11 BODIPY-positive cell populations. (D) C11-BODIPY staining of HT-1080 cells treated with ferroptosis modulators and cotreated with 0 or 6 Gy radiation measured by flow cytometry. **$p < 0.01$. (E) Glutathione (GSH) level is detected in HT-1080 cells treated with DMSO or IKE and cotreated with radiation for 24 h using a fluorometric assay. ****$p < 0.0001$, **$p < 0.01$, *$p < 0.05$, n.s.: $p > 0.05$. Data are plotted as mean ± SEM; $n = 3$ technical replicates for A, B, D, and E. Three biologically independent experiments were performed with similar results.

(RSL3), a GPX4 inhibitor, which are both small-molecule inducers of ferroptosis. We tested their ability to prevent clonogenic growth, along with DMSO-treated controls. The colony-forming ability of cells was measured, and the dose responses to radiation of DMSO-treated, IKE-treated, and RSL3-treated groups were compared (Figure 1A). Both IKE and

https://dx.doi.org/10.1021/acschembio.9b00939
ACS Chem. Biol. XXXX, XXX, XXX−XXX

RSL3 significantly enhanced the effects of radiation in decreasing clonogenic survival. Given that radiation also induces apoptosis, necroptosis, and autophagy in different contexts, we also tested whether inducers of alternative cell death pathways could synergize with radiation under similar conditions. We found that the apoptosis inducers staurosporine and doxorubicin, the autophagy inducer rapamycin, and induction of necroptosis using a combination of TNFα, Z-VAD-FMK, and birinapant[17] were capable of only slightly enhancing radiation-induced cell death (Figure S1A), to a lesser degree than the enhancement observed using IKE and RSL3.

The coefficient of drug interaction (CDI), used to compute interaction between two drugs, was used to quantify synergy between cell death inducers and radiation according to the formula CDI = AB/(A × B), where AB is the surviving fraction of the combination treatment, and A and B are the surviving fractions of the individual treatments. CDI < 1 indicates synergy. CDI = 1 indicates additivity, and CDI > 1 indicates antagonism[18] (Table S1). The results indicate that ferroptosis inducers synergize with radiation to a greater degree than other compounds in HT-1080 cells and suggest that, although a variety of mechanisms may participate in radiation-induced cell death in this model system, ferroptosis is the most pronounced.

We then tested whether cell death enhancement of radiation with ferroptosis inducers occurred across diverse tumor cell types. Using the same assay, we evaluated several cancer cell lines for synergistic cell killing with radiation and either IKE or RSL3 (Figure S1B−E). In addition to the initial ferroptosis-sensitive HT-1080 sarcoma cell line, glioma and lung cancer cells were evaluated, due to the clinical relevance of radiation therapy for its treatment. Enhanced cell killing was observed in all cell lines, SK-LMS-1 (uterine sarcoma), U87 (primary glioblastoma), and A549 and PC9 (lung carcinomas) when combining radiation with a ferroptosis inducer. The CDI values for each cell line were recorded at various doses of radiation and ferroptosis inducers, and the maximal CDI for each cell line was compared (Figure 1B and Table S2). The interactions between radiation and both ferroptosis inducers were synergistic for all the cell lines, ranging from CDI = 0.70 for IKE with radiation in PC9 cells to CDI = 0.09 for RSL3 with radiation in HT-1080 cells. Taken together, the results suggest that the cancer cell lines derived from radiation-sensitive tumors are synergistically killed by IKE and RSL3 and irradiation.

Radiation-Induced Cancer Cell Death Is Suppressed by Ferroptosis Inhibitors. It has been reported that radiation causes lipid peroxidation in cells,[11] in addition to its widely known ability to induce DNA damage. Thus, we hypothesized that cell death caused by radiation alone may partially be due to ferroptosis, particularly in contexts in which DNA damage does not induce apoptosis. To test this, we measured the effect of ferroptosis inhibitors ferrostatin-1 and deferoxamine, as well as the apoptosis inhibitor Z-VAD-FMK, on the colony-forming ability of HT-1080 cells treated with 1, 2, or 4 Gy radiation alone. In this experiment, the lipophilic radical-trapping agent and ferroptosis inhibitor ferrostatin-1 significantly rescued colony formation, whereas the apoptosis inhibitor Z-VAD-FMK did not (Figure 1C). Deferoxamine (DFO), a ferroptosis inhibitor and iron chelator, prevented cell proliferation and colony formation independent of radiation treatment, likely due to the requirement for iron for cell proliferation (data not shown). We then seeded cells more densely and measured short-term cell viability with an ATP-based luciferase assay to bypass this effect of DFO; cells treated with 4 Gy radiation for 24 h were rescued from death by cotreatment with either DFO or ferrostatin-1, but not by cotreatment with Z-VAD-FMK or with the necroptosis inhibitor necrostatin-1S (Figure 1D). The autophagy inhibitor 3-methyladenine also rescued cells in this format, suggesting that autophagy may also contribute to radiation-induced cell death in this model. Given that several autophagy-related genes are positive regulators of ferroptosis, one speculative explanation is that inhibiting autophagy also limits NCOA4-dependent ferritinophagy, therefore limiting intracellular redox-active iron availability and downregulating ferroptosis.[19]

We then evaluated whether the observed synergy in cell killing between radiation and ferroptosis inducers was due to enhanced ferroptosis. In this set of colony formation assays, we treated HT-1080 cells with the same doses of radiation and ferroptosis inducers, in the presence or absence of ferroptosis inhibitors ferrostatin-1 or trolox (Figure 1E−H). Both of these lipophilic radical-trapping agents (which protect lipid membranes from oxidation) acted to suppress the synergy observed between either IKE or RSL3 and radiation. Consistent with the previous experiments, both inhibitors also partially rescued cell death induced by radiation alone, in the absence of ferroptosis inducers. These results suggest that ferroptosis and lipid peroxidation contribute to radiation-induced cell death in HT-1080 cells, and that this ferroptotic cell death can be enhanced by the addition of otherwise sublethal concentrations of IKE or RSL3.

Genetic and Biochemical Hallmarks of Ferroptosis Are Observed in Radiation-Treated Cancer Cells. On the basis of the above results, we sought to evaluate further whether ferroptosis is a mechanism for radiation-induced cell death and IKE/RSL3-amplified death in these cells. To this end, we measured the mRNA expression level of prostaglandin-endoperoxide synthase 2 (*PTGS2*), a pharmacodynamic biomarker of ferroptosis,[15] using RT-qPCR in HT-1080 cells that were (1) radiated alone, (2) treated with 100 nM RSL3, (3) radiated and cotreated with RSL3, or (4) radiated and cotreated with 10 μM ferrostatin-1. We found that after 24 h, *PTGS2* mRNA was significantly induced in cells that were treated with 6 Gy radiation when compared to untreated cells (Figure 2A). Treating cells with ferrostatin-1 in combination with radiation reversed this induction of *PTGS2*. When radiation was combined with RSL3, the upregulation in *PTGS2* mRNA was even further enhanced.

Next, we sought to test the effects of radiation on cell membrane lipid peroxidation in a ferroptosis-sensitive cell context. We quantified levels of malondialdehyde (MDA), a biomarker for lipid peroxidation and ferroptosis, using an assay that measures thiobarbituric acid reactive substances (TBARS).[20] In this assay, thiobarbituric acid (TBA) was added to cell lysates and heated under acidic conditions to form the MDA-TBA adduct, which was measured colorimetrically. MDA levels were found to be significantly elevated in cells treated for 24 h with 1 μM IKE, 6 Gy radiation, or a combination of the two, when compared to untreated cells (Figure 2B). Cells treated with 10 μM ferrostatin-1, either in the presence or absence of radiation, showed significantly lower levels of MDA compared to control cells.

To confirm that radiation causes lipid peroxidation in these cells, lipid peroxidation was also measured with C-11 BODIPY (581/591), a membrane-targeted lipid sensor dye. Flow cytometry analysis of HT-1080 cells treated with radiation, ferroptosis inducers, or a combination of both for 24 h and

https://dx.doi.org/10.1021/acschembio.9b00939
ACS Chem. Biol. XXXX, XXX, XXX−XXX

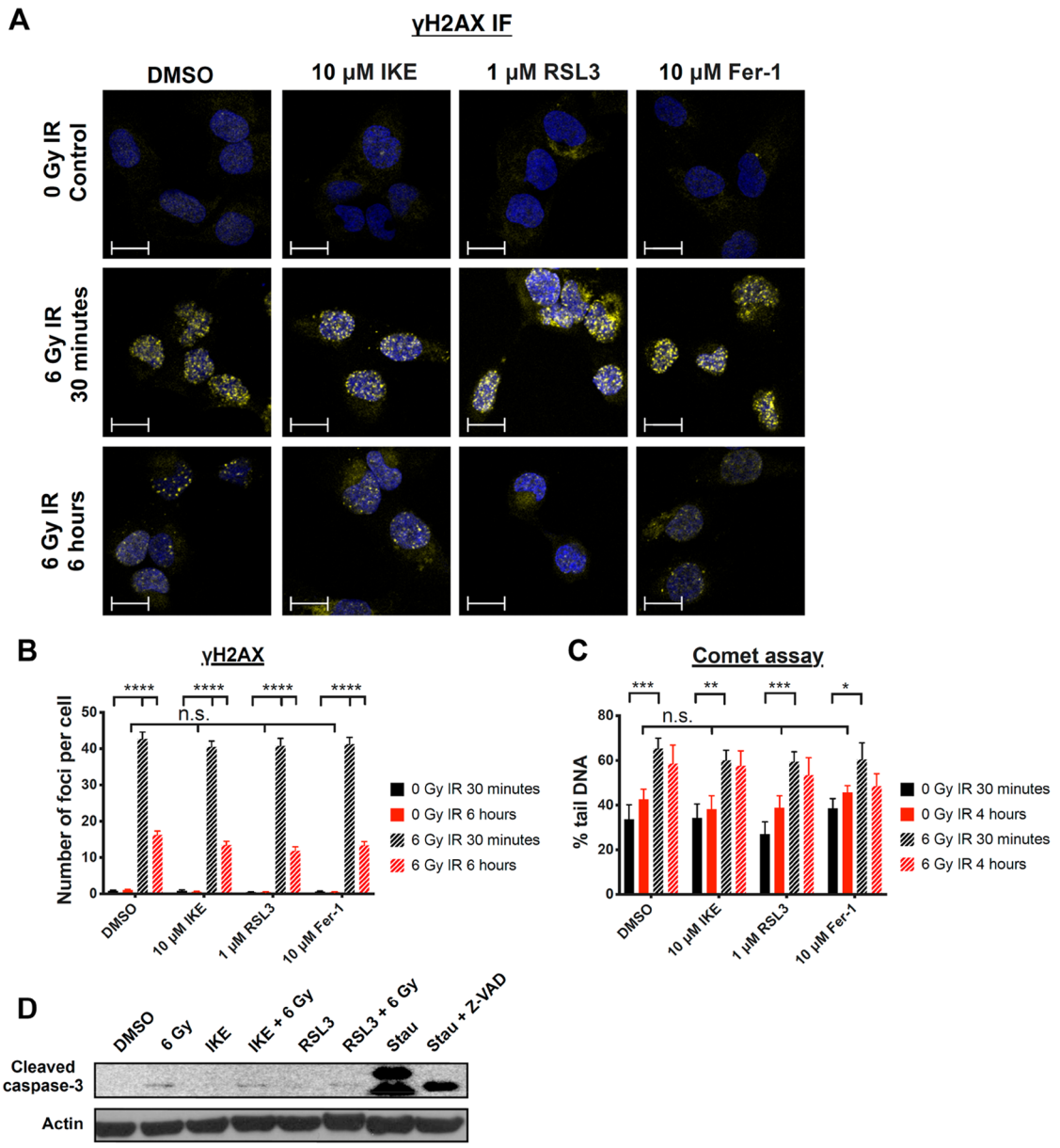

Figure 3. Enhancement of radiation-induced cell death by IKE and RSL3 in HT-1080 cells through mechanisms independent of DNA damage or apoptosis. (A) Representative images of γH2AX immunofluorescence staining in HT-1080 cells treated with DMSO, IKE, RSL3, or ferrostatin-1 and cotreated with 0 or 6 Gy radiation for 30 min or 6 h. Blue, DAPI; yellow, γH2AX-FITC. Scale bar, 10 μm. (B) Quantification of γH2AX immunofluorescence staining in HT-1080 cells treated with DMSO, IKE, RSL3, or ferrostatin-1 and cotreated with 0 or 6 Gy radiation for 30 min or 6 h. ****$p < 0.0001$, n.s.: $p > 0.05$. (C) Quantification of percent tail DNA in HT-1080 cells using the comet assay. Cells were treated with DMSO, IKE, RSL3, or ferrostatin-1 and cotreated with 0 or 6 Gy radiation for 30 min or 4 h. ***$p < 0.001$, **$p < 0.01$, *$p < 0.05$, n.s.: $p > 0.05$. (D) Western blot of cleaved caspase-3 in HT-1080 cells treated with DMSO, 1 μM IKE, or 50 nM RSL3 and cotreated with 0 or 6 Gy radiation for 24 h. Cells treated with 500 nM staurosporine and 500 nM staurosporine + 100 μM Z-VAD-FMK were included as positive and negative controls. Data are plotted as mean ± SEM. Three biologically independent experiments were performed with similar results for B, C, and D.

stained with C11-BODIPY showed that the combination treatment of either 1 μM IKE or 50 nM RSL3 with 6 Gy radiation significantly increased C-11 BODIPY fluorescence when compared to either radiation or a ferroptosis inducer alone (Figure 2C,D). The resulting enhancement was reversed in both cases by also cotreating the cells with ferrostatin-1.

Ferroptosis inducers have been shown to alter the availability and consumption of intracellular glutathione (GSH). Class I ferroptosis inducers, such as IKE, inhibit system x_c^-, the cystine/glutamate antiporter on the plasma membrane that exchanges intracellular glutamate and extracellular cystine.[12,14,21] Cystine taken up by system x_c^- is reduced to cysteine, a building block in the biosynthesis of glutathione. The glutathione-depleting effect of IKE is thought to be its main mechanism of action that drives ferroptosis. Using a fluorometric GSH probe, we observed that treatment with 2 or 6 Gy radiation for 24 h depleted GSH in a dose-dependent manner in HT-1080 cells (Figure 2E). In addition, levels of glutathione further decreased when irradiated cells were cotreated with 2 μM IKE, suggesting that the two processes work in a cooperative fashion to deplete GSH. Indeed, the decrease in colony formation of HT-1080 cells following 2 or 4 Gy radiation was rescued by either glutathione methyl ester or

https://dx.doi.org/10.1021/acschembio.9b00939
ACS Chem. Biol. XXXX, XXX, XXX−XXX

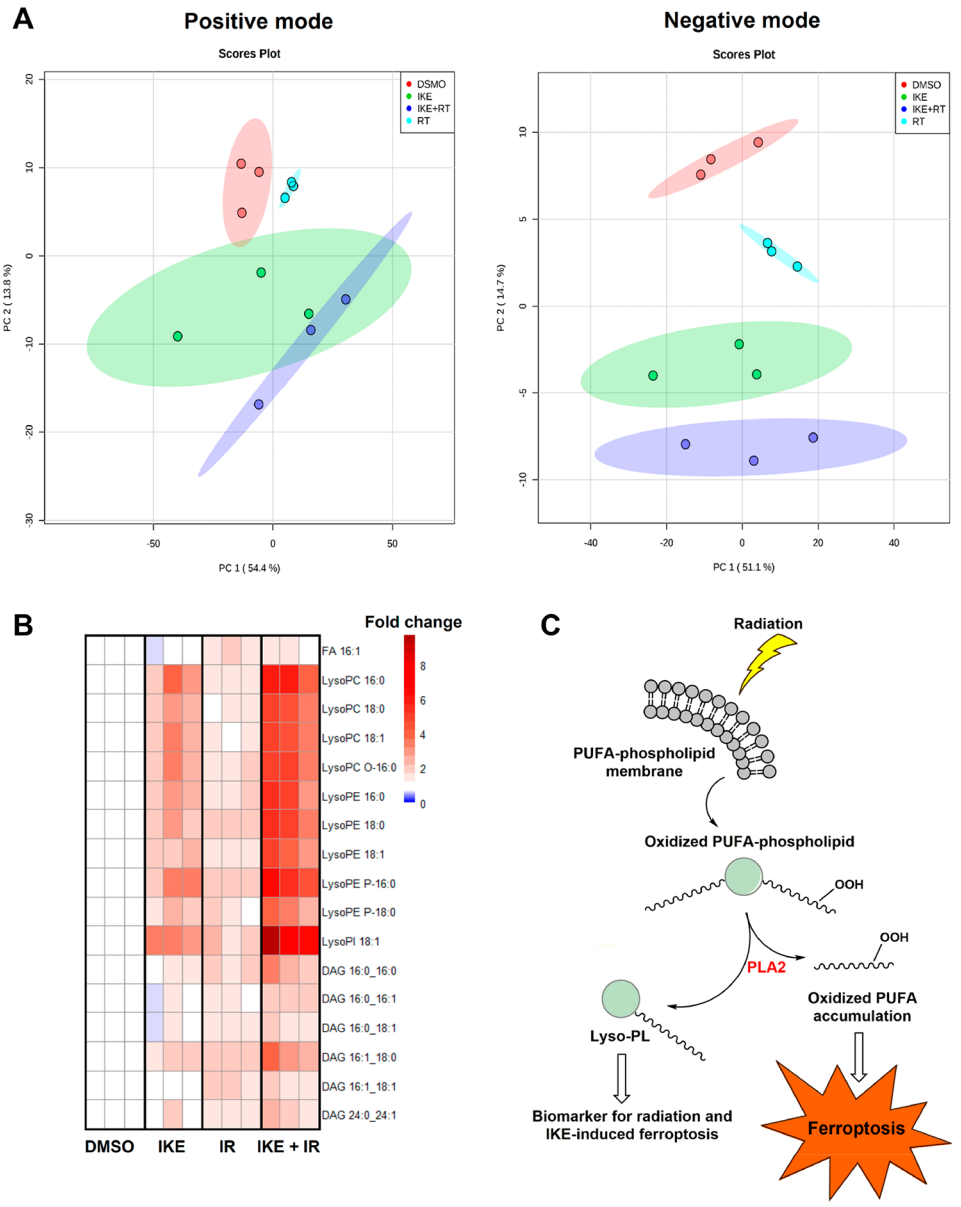

Figure 4. Enhanced ferroptosis lipid signatures in cells cotreated with IKE and radiation in HT-1080 cells revealed by untargeted lipidomic study. (A) Principal component analysis of the extracted lipid features in samples treated with DMSO or 5 μM IKE for 12 h, with or without 6 Gy radiation for 24 h, in both positive and negative electrospray ionization modes. (B) Fold change heatmap of significantly changed lipid features from both IKE treatment and radiation treatment determined by two-way ANOVA (FDR corrected p value <0.05) combined from both positive and negative ionization modes. Blue indicates decreased abundance compared to DMSO-treated controls (fold changes between 0.3 and 0.8). White indicates no change (fold changes between 0.8 and 1.2). Red indicates increased abundance (fold changes between 1.2 and 10). n = 3 biologically independent samples. Abbreviations: FA, fatty acid; LysoPC, lysophosphatidylcholine; LysoPE, lysophosphatidylethanolamine; LysoPI, lysophosphatidylinositol; DAG, diacylglycerol. (C) Proposed model of how oxidation of membrane polyunsaturated fatty acids by IKE and radiation causes elevated lysophospholipids and cell death. Abbreviations: PUFA, polyunsaturated fatty acid; PLA2, phospholipase A2; Lyso-PL, lysophospholipid.

N-acetylcysteine, which is a biological precursor to glutathione (Figure S2). This finding provides a potential mechanism by which radiation and IKE act together to cause increased cell death.

IKE and RSL3 Do Not Enhance Radiation-Induced DNA-Damage Signaling. Mechanisms of the cellular lethality from radiation are thought to be mainly derived from the downstream caspase-dependent apoptosis induced by DNA damage, including complex double-strand DNA breaks.[2,22] Therefore, we wanted to determine if ferroptosis inducers and radiation induce DNA damage or affect DNA repair. We evaluated the extent of these effects of radiation by measuring DNA breaks and caspase activation in HT-1080 cells cotreated with radiation and ferroptosis inducers. Immunofluorescence staining of γH2AX, a marker for double-strand DNA (dsDNA) damage and repair, was performed in cells treated with 10 μM IKE, 1 μM RSL3, or 10 μM ferrostatin-1 along with DMSO control (Figures 3A,B). The cells were either treated with radiation (6 Gy) or not irradiated (0 Gy) as a control. After 30 min, numerous γH2AX foci were present in irradiated cells but absent in control cells, suggesting that, as expected, radiation at this dose caused significant DNA damage.

https://dx.doi.org/10.1021/acschembio.9b00939
ACS Chem. Biol. XXXX, XXX, XXX−XXX

However, pharmacological modulators of ferroptosis did not affect the number of observed γH2AX foci in any of the treatment groups, indicating that ferroptosis inducers alone do not cause double-strand DNA breaks, and that this type of DNA damage does not correlate with the radiation-sensitizing effects of IKE and RSL3, nor with the rescuing effect of ferrostatin-1, toward radiation-induced cell death. An experiment was then performed at 6 h post-treatment, at which point the majority of the γH2AX foci in cells treated with radiation alone disappeared, presumably due to DNA repair. Similarly, no differences were observed between the irradiated groups treated with the vehicle DMSO and those treated with IKE, RSL3, or ferrostatin-1, which suggested that DNA repair was not delayed by the cotreatment with ferroptosis inducers, nor enhanced by the cotreatment with ferrostatin-1. Treatment with IKE or RSL3 alone for 6 h did not result in γH2AX foci formation, with results similar to the 30 min treatment. These results demonstrate that double-stranded DNA breaks do not correlate with the effects of ferroptosis inducers on cell viability in HT-1080 cells.

To test for other forms of DNA damage that cannot be detected by the γH2AX assay, we performed a comet assay, which detects single strand DNA damage in addition to double strand breaks, in HT-1080 cells treated under the same conditions. After 30 min, we observed a significant difference in percent of tail DNA between irradiated and unirradiated groups, demonstrating that DNA breaks had occurred following radiation treatment. We did not detect a significant increase in DNA single strand damage in cells treated with IKE or RSL3 alone, and no significant enhancement of DNA damage when IKE or RSL3 was combined with radiation, even when a proportion of cells had started to die at the 4 h time point (Figure 3C). We also did not observe a significant protective effect of ferrostatin-1 toward radiation-induced DNA single strand damage. These results again reinforce the conclusion that although DNA damage occurs in HT-1080 cells exposed to radiation, it is not related to the synergistic cell death observed during cotreatment with ferroptosis inducers.

DNA damage is a potent inducer of apoptosis. Therefore, we also tested for the presence of radiation-induced apoptosis by measuring levels of cleaved caspase-3 in HT-1080 cells treated with 6 Gy radiation, or with IKE or RSL3, or with a combination of radiation plus ferroptosis inducer, for 24 h (Figure 3D). Levels of cleaved caspase-3 were minimally elevated in cells treated with radiation compared with those of nonirradiated cells, and the addition of ferroptosis inducers did not further increase the amount of cleaved caspase-3. Treatment with ferroptosis inducers alone did not induce detectable cleavage of caspase-3, as previously reported.[23] In contrast, the pro-apoptosis inducer staurosporine, used as a positive control at 500 nM for 6 h, induced cell death along with levels of caspase-3 cleavage, shown by bands at 17 and 19 kDa. When these cells were cotreated with staurosporine and 100 μM Z-VAD-FMK, a pan caspase inhibitor, the cells were rescued from staurosporine-induced cell death. Despite this, some quantity of 17-kDa cleaved caspase-3 was still detectable in the Z-VAD-FMK-treated sample. To further check for potential radiation-induced apoptosis in this model at a later time point, we attempted to rescue the effects of radiation using 100 μM Z-VAD-FMK after 48, 72, and 96 h (Figure S3). However, no significant rescue of cell viability was observed at any of these time points.

These findings suggest that ferroptosis driven by lipid peroxidation, not DNA damage or apoptosis, is the predominant radiosensitizing mechanism of ferroptosis inducers in HT-1080 cells.

Untargeted Lipidomics Reveals Molecular Features of Ferroptosis in Cells Cotreated with IKE and Radiation. To further probe the effects of radiation on cellular lipid composition and metabolism in cells that are ferroptosis-sensitive, we performed ultraperformance liquid chromatography coupled to quadrupole-time-of-flight-mass-spectrometry-(UPLC-q-ToF MS-)based untargeted lipidomics analysis of HT-1080 cells treated with 0 or 6 Gy radiation for 24 h and cotreated with either DMSO vehicle or 5 μM IKE for 12 h. Untargeted UPLC-MS analyses of the samples resulted in the detection of 1304 and 561 features in the positive and negative electrospray ionization (ESI) modes, respectively. Unsupervised principal component analysis of the detected lipid features in both ESI modes showed clear clustering and separation among the groups (Figure 4A). Using two-way ANOVA (FDR corrected p value < 0.05 for both IKE-treated and IR-treated samples when compared to control samples), we found 18 lipid ions in the positive and 10 lipid ions in the negative ESI modes whose abundances changed significantly among the groups (Table S3). By integrating the annotated lipid ions in both modes, we found 17 unique lipid species, including one free fatty acid (FA 16:1), 10 lysophospholipids (LysoPLs), and six diacylglycerols (DAGs), which increased significantly in cells treated with IKE or radiation, with even larger increases when IKE and radiation were combined (Figure 4B). Lysophospholipids, molecules generated following PUFA-containing phospholipid peroxidation by enzymatic cleavage of the oxidized PUFA tail, have been implicated in oxidative stress and accumulate during treatment with ferroptosis inducers.[16,24,25] Among these, lysophosphatidylinositol 18:1 (LysoPI 18:1; interaction p value = 0.01) and lysophosphatidylethanolamine 18:1 (LysoPE 18:1; p = 0.03) in particular had significantly interacting synergistic effects between IKE and radiation. Furthermore, the significantly elevated levels of diacylglycerols may have resulted from hydrolysis of triacylglycerols, which are enriched in ferroptosis-sensitive cell states of clear-cell carcinoma and have been shown to be accumulated by IKE in cell culture models of diffuse large B-cell lymphoma.[16,26] Of these, DAG 16:0_16:1 also displayed significant interaction between IKE and radiation (p < 0.05).

These results suggest that radiation-driven lipid peroxidation in ferroptosis-sensitive cells produces a downstream lipid signature similar to that produced by IKE alone and consistent with the previous studies of cell lipidome changes during ferroptosis. In combination therapy, the oxidation of PUFA-phospholipids by radiation enhances the same effect driven by IKE, presumably potentiating ferroptosis through the accumulation of oxidized PUFAs and producing lysophospholipids as a byproduct that are a ferroptosis biomarker (Figure 4C). However, the exact role of lysophospholipids in ferroptosis remains unexplored. We next utilized a precision charged particle microbeam to elucidate the consequence of lipid peroxidation with irradiation of subcellular compartments.

Targeted Cytoplasmic, but Not Nuclear, Microbeam Radiation Selectively Synergizes with IKE and RSL3 to Enhance Clonogenic Cell Death. To further probe the mechanism by which radiation synergizes with IKE and RSL3 to cause cell death, we used a 5-MeV proton microbeam to deliver targeted radiation to either the nucleus or the cytoplasm of HT-1080 cells.[27] The microbeam consists of a single beam of proton radiation with a spot size of 4 μm that allows radiation damage to

https://dx.doi.org/10.1021/acschembio.9b00939
ACS Chem. Biol. XXXX, XXX, XXX−XXX

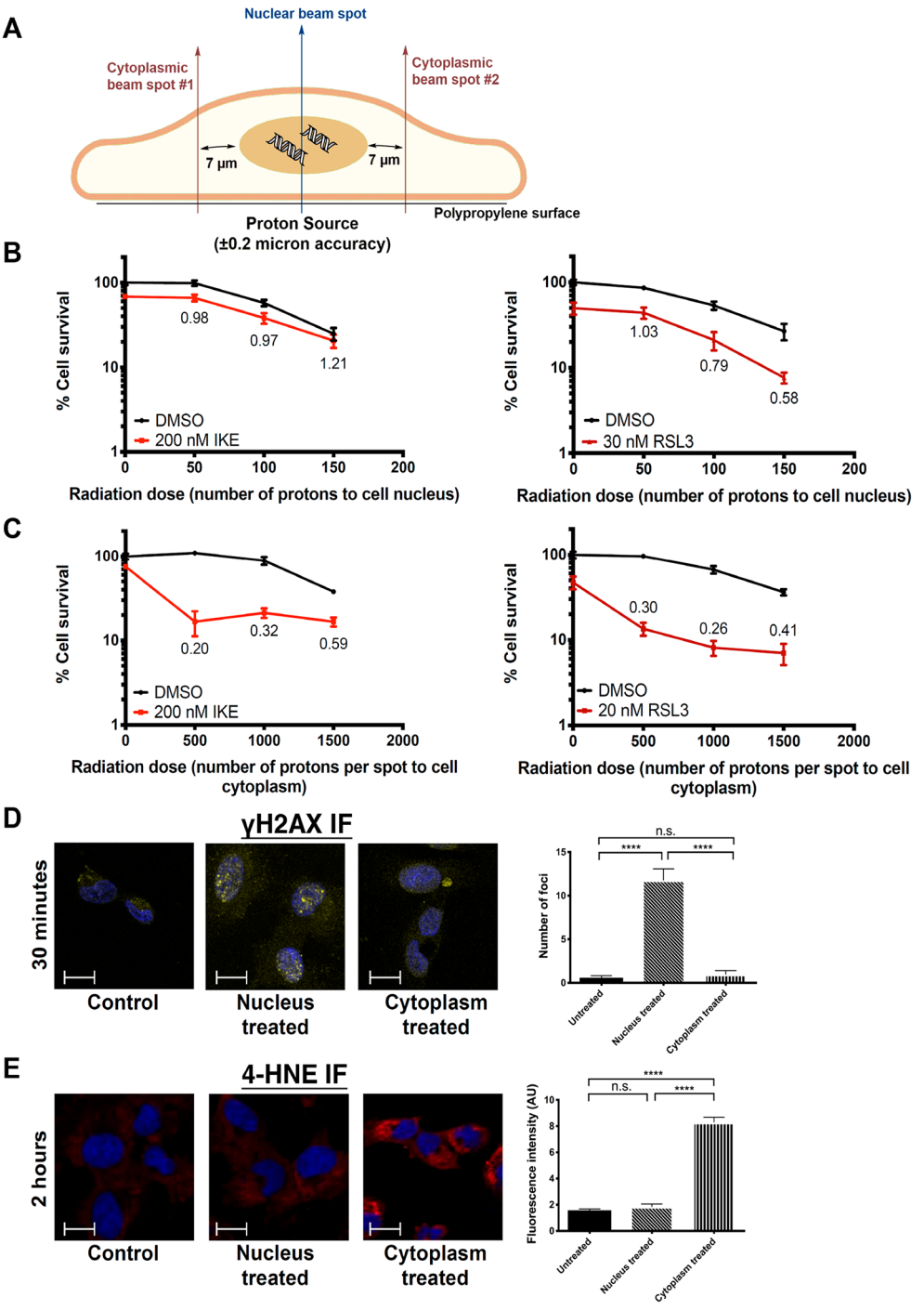

Figure 5. Synergism of ferroptosis inducers with cytoplasmic irradiation but not nuclear irradiation in HT-1080 cells. (A) Diagram of microbeam setup showing locations of beam spots targeting either the nucleus or cytoplasm. (B) Clonogenic cell survival of HT-1080 cells treated with nuclear radiation and IKE or RSL3. CDI values are indicated. (C) Clonogenic cell survival of HT-1080 cells treated with cytoplasmic radiation and IKE or RSL3. CDI values are indicated. (D) Immunofluorescence staining of γH2AX in untreated cells and cells treated with 100 protons to the nucleus or 2000 protons to the cytoplasm for 30 min. Blue, DAPI; yellow, γH2AX-FITC. ****$p < 0.0001$, n.s.: $p > 0.05$. Scale bar, 10 μm. (E) Immunofluorescence staining of 4-HNE in untreated cells and cells treated with 100 protons to the nucleus or 2000 protons to the cytoplasm for 2 h. Blue, DAPI; red, 4-HNE-Rhodamine Red. ****$p < 0.0001$, n.s.: $p > 0.05$. Scale bar, 10 μm. Data are plotted as mean ± SEM; $n = 3$ side-by-side experiments. Three biologically independent experiments were performed with similar results.

be precisely deposited at specific locations in a cell. This translates to delivery of a precise number of protons to either the cell nucleus or to the cytoplasm outside of the nucleus.[28,29] The targetable nature of the microbeam allows us to distinguish the cytoplasmic effects of radiation from its nuclear effects, and test if the former is the predominant component that drives radiation-induced ferroptosis. To target the microbeam, cells were labeled with Hoechst stain and imaged. Nuclear radiation was delivered to the center of gravity of the cell nucleus, whereas cytoplasmic radiation was delivered to two sites 7 μm away from the nuclear edge along the nuclear long axis (Figure 5A). Using this method, we first established dose responses of these cells to

https://dx.doi.org/10.1021/acschembio.9b00939
ACS Chem. Biol. XXXX, XXX, XXX−XXX

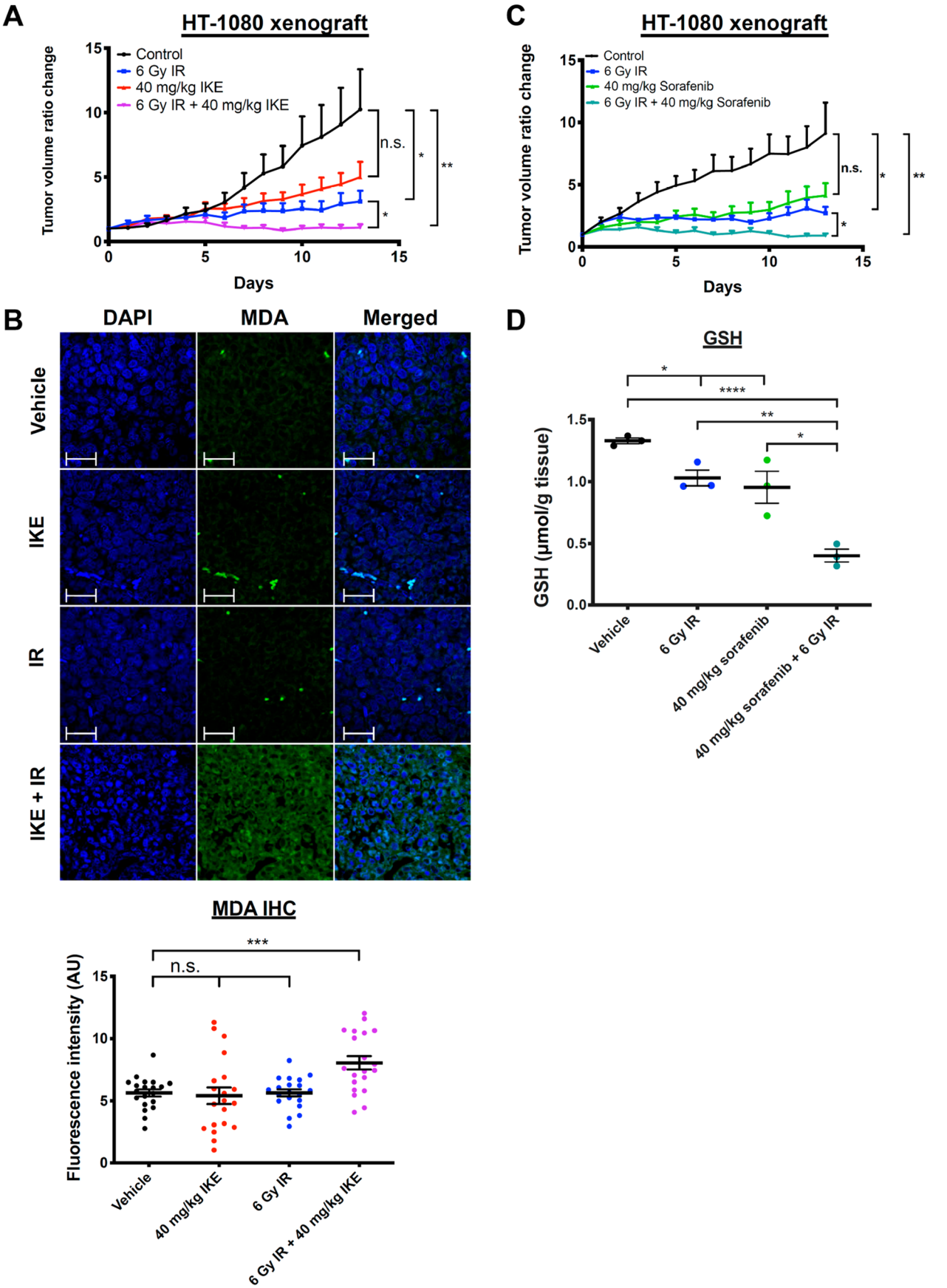

Figure 6. Suppression of tumor growth in a mouse xenograft model of sarcoma and a patient-derived xenograft model of lung adenocarcinoma with IKE and sorafenib, combined with stereotactic radiation therapy. (A) Tumor volume ratio change in HT-1080 xenograft tumors treated with vehicle or

https://dx.doi.org/10.1021/acschembio.9b00939
ACS Chem. Biol. XXXX, XXX, XXX−XXX

Figure 6. continued

IKE for 14 days and cotreated with 0 or 6 Gy radiation on days 2 and 4. n = 7 or 8 mice per group. $^{**}p < 0.01$, $^{*}p < 0.05$, n.s.: $p > 0.05$. (B) Immunofluorescence staining and quantification of MDA on paraffin-embedded tumor tissue sections measured by confocal microscopy. Blue, DAPI; green, MDA-FITC. Scale bar, 50 μm. $^{***}p < 0.01$, n.s.: $p > 0.05$. n = 20 images with sections cut from four randomly chosen mice from each group, and five images captured from each section. (C) Tumor volume ratio change in HT-1080 xenograft tumors treated with vehicle or sorafenib for 14 days and cotreated with 0 or 6 Gy radiation on days 1 and 3. n = 4 or 5 mice per group. $^{**}p < 0.01$, $^{*}p < 0.05$, n.s.: $p > 0.05$. (D) Glutathione (GSH) level is detected in HT-1080 xenograft tumors treated with vehicle or sorafenib for 14 days and cotreated with 0 or 6 Gy radiation on days 1 and 3, using a fluorometric assay. $^{****}p < 0.0001$, $^{**}p < 0.01$, $^{*}p < 0.05$. n = 3 tumor samples from different animals per group.

nuclear and cytoplasmic radiation. The ED_{50} for clonogenic cell death was observed to be around 100 protons for nuclear radiation, and between 1000 and 1500 protons per site for cytoplasmic radiation (Figure S4). Compared to conventional photon radiation, these doses approximately correspond to 1 Gy to the nucleus and between 1 and 5 Gy to the cytoplasm, a therapeutically relevant dose range that is consistent with our previous experiments. Similar to previous reports, these results suggest that nuclear proton radiation was more lethal to cells than cytoplasmic proton radiation, presumably through direct radiation-induced damage to DNA and genome integrity.[30] This supports the view that the genotoxic effects of radiation are attributed mainly to direct damage to the nucleus.

However, when microbeam radiation was combined with inducers of ferroptosis, we observed that nuclear radiation had no synergy with IKE and RSL3, whereas cytoplasmic radiation synergized strongly with both compounds (Figure 5B,C). Notably, although no significant cell death was observed with 500 or 1000 protons alone delivered per site to the cytoplasm, there was a large decrease in cell survival when irradiated cells were concurrently treated with sublethal doses of either of the two ferroptosis inducers, leading to synergistic CDI values between 0.2 and 0.4. By comparison, no such effect was observed when the cells were treated with nuclear irradiation. These results suggest that ferroptosis inducers sensitize cells to the effects of radiation primarily in the cytoplasm.

To further highlight the differences between nuclear and cytoplasmic microbeam radiation, and to examine if they represent two distinct forms of radiation-induced cell death, we sought to measure levels of DNA damage and lipid peroxidation in cells treated under the two conditions. To measure DNA damage, cells were treated either with 100 protons to the nucleus or 2000 protons to each site in the cytoplasm. γH2AX immunofluorescence staining for dsDNA breaks was performed 30 min postirradiation (Figure 5D). γH2AX foci were indeed present in cells treated with nuclear radiation, but absent from cells treated with cytoplasmic radiation. To examine the microbeam's effects on lipid peroxidation, we performed immunofluorescence staining of 4-hydroxynonenal (4-HNE), a marker of lipid peroxidation, in cells with the same treatment conditions at 2 h postirradiation (Figure 5E). The 4-HNE signal was significantly increased in samples treated with cytoplasmic radiation relative to untreated cells, but not in those treated with nuclear radiation.

Taken together, these findings indicate that, although damage to the nucleus remains an important mechanism of radiation therapy in some contexts, inducers of ferroptosis serve to activate a distinct cell death mechanism based in the cytoplasm, which may become relevant in cancer cells that have acquired resistance to the traditional cell death and DNA damage pathways. Although it is not possible to differentially deliver cytoplasmic vs nuclear radiation in clinical contexts, the microbeam is nevertheless a useful tool to separate the effects of radiation-induced lipid peroxidation and DNA damage and to examine how ferroptosis synergizes with the former but not the latter in different cells and tumors. Further mechanistic studies may reveal the targets contained within the cytoplasm required for this synergy, which could in principle be pharmacologically modulated for downstream clinical applications.

IKE and Sorafenib Enhance Effects of Radiation to Inhibit Tumor Growth in a Xenograft Mouse Model of Sarcoma. We sought to evaluate the efficacy of the combined treatment regimen of radiation and ferroptosis inducer in an *in vivo* tumor model. Of the two ferroptosis inducers tested in the cell culture, IKE was selected for *in vivo* studies due to its previously established stability and activity in xenograft mouse models of cancer.[16] Athymic nude mice were implanted with subcutaneous HT-1080 fibrosarcoma cells to form xenograft tumors. When the tumors reached an average volume of approximately 100 cubic millimeters, intraperitoneal (i.p.) injections of 40 mg/kg IKE or vehicle were delivered daily for 14 days, starting on day 0 and ending on day 13. On days two and four of IKE treatment, 0 or 6 Gy radiation was delivered to the tumor site using the Small Animal Radiation Research Platform (SARRP) system.[31] After 2 weeks, tumor volume was compared between mice treated with vehicle, IKE alone, radiation alone, or a combination of both (Figure 6A). Using two-sample t tests, we observed a significant difference between the vehicle-treated control group and the groups treated with radiation alone; IKE alone was not strongly effective at this dose level in this model. We observed a significant further reduction in tumor volume between the single treatment groups when compared to the group treated with combination therapy, showing that IKE enhanced the effects of radiation in reducing tumor growth. Upon analysis of all groups with the two-way ANOVA test, we found statistical significance for treatment with IKE alone (p = 0.03) and radiation alone (p = 0.004). The two factors interacted positively with each other, although the interaction p value did not reach significance (p = 0.34).

Using weight loss as a measure of mice health, we did not observe any significant differences between any of the groups for the duration of the experiment (Figure S5A). This suggests that IKE and radiation and the combination were well tolerated at these dose levels for this length of exposure.

Next, we measured malondialdehyde (MDA) levels, as a biomarker for ferroptosis, in tumor tissue using immunohistochemistry on fixed and paraffin-embedded tumor samples resected at day 14 post-treatment (Figure 6B). We observed significantly elevated MDA signal in tumors treated with both IKE and radiation compared to that of tumors treated with vehicle, suggesting enhanced lipid peroxidation and ferroptosis in the cotreated tumors. No significant differences were observed between tumors treated with vehicle, IKE only, or radiation only. This again suggests a synergistic pharmacodynamic effect of radiation and IKE in this tumor model.

https://dx.doi.org/10.1021/acschembio.9b00939
ACS Chem. Biol. XXXX, XXX, XXX−XXX

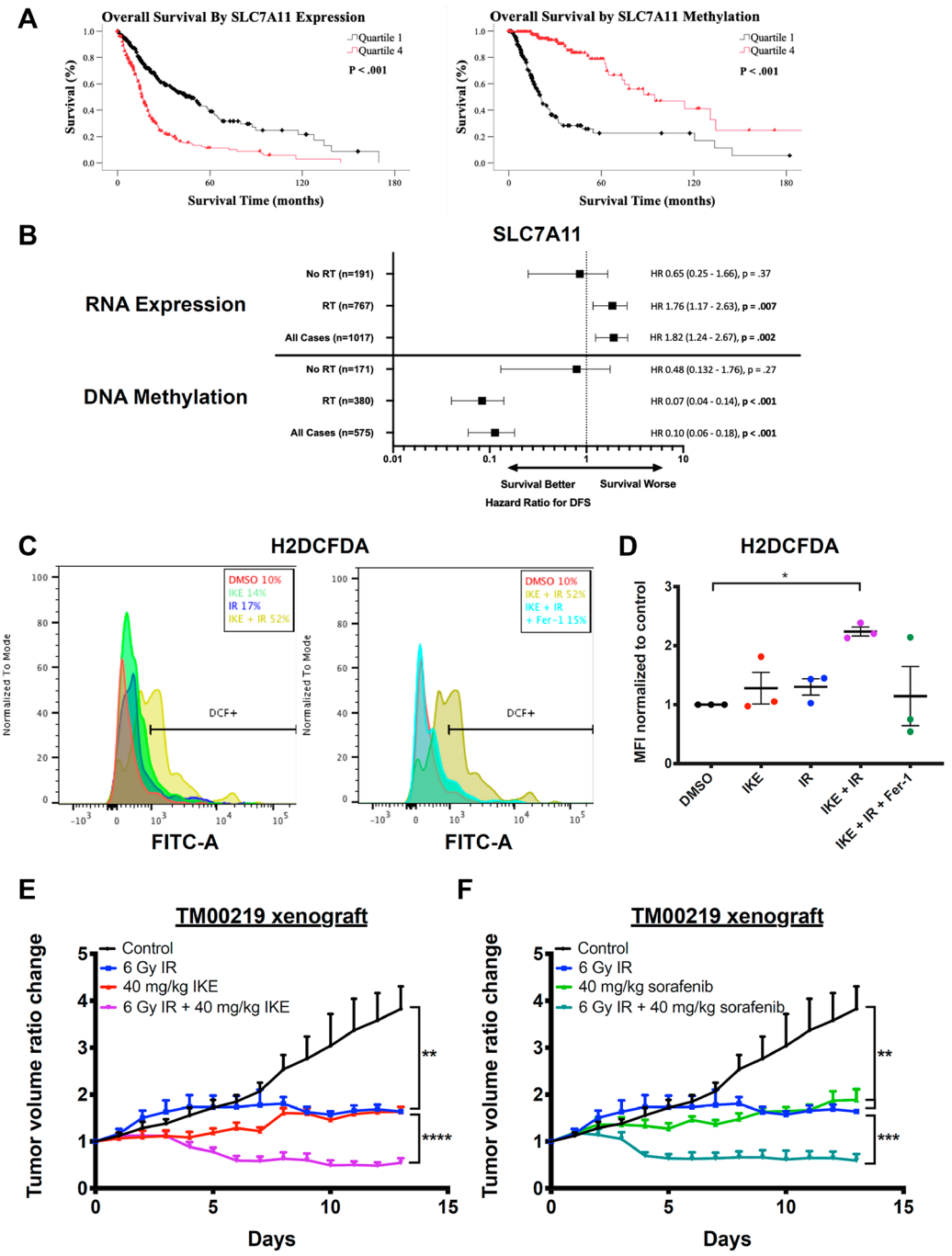

Figure 7. SLC7A11, a target for radiosensitization in human models of glioma and lung adenocarcinoma. (A) Kaplan−Meier survival analysis of overall survival of TCGA glioma patients in quartile 1 (low) and quartile 4 (high) of SLC7A11 RNA expression (left) or DNA methylation (right). (B) Hazard ratios for disease-free survival between patients in quartile 1 (low) and quartile 4 (high) of SLC7A11 RNA expression or DNA methylation either in the case of radiation treatment, no radiation treatment, or all cases. (C) Representative histograms of a human diffuse astrocytoma slice culture sample treated with DMSO, 10 μM IKE, or 10 μM IKE + 10 μM ferrostatin-1, cotreated with 0 or 2 Gy radiation for 24 h, dissociated, stained with H2DCFDA, and measured by flow cytometry. Horizontal bars indicate H2DCFDA-positive cell populations. (D) H2DCFDA staining of three human glioma slice culture samples treated with DMSO, 10 μM IKE, or 10 μM IKE + 10 μM ferrostatin-1, cotreated with 0 or 2 Gy radiation for 24 h, dissociated, stained with H2DCFDA, and measured by flow cytometry. *$p < 0.05$. $n = 3$ samples from different human glioma patients. (E) Tumor volume ratio change in TM00219 patient-derived xenograft tumors treated with vehicle or IKE for 14 days and cotreated with 0 or 6 Gy radiation on day 1. $n = 5$ or 6 mice per group. ****$p < 0.0001$, **$p < 0.01$. (F) Tumor volume ratio change in TM00219 patient-derived xenograft tumors treated with vehicle or sorafenib for 14 days and cotreated with 0 or 6 Gy radiation on day 1. $n = 5$ or 6 mice per group. ***$p < 0.001$, **$p < 0.01$. Data are plotted as mean ± SEM.

We then sought to test the radiosensitizing effect of sorafenib, an FDA-approved chemotherapeutic drug, which also acts as an inhibitor of system x_c^-.[21] First, the colony-forming ability of HT-1080 cells when treated with sorafenib, radiation, or a combination was compared to that of untreated cells. We found that treatment with 5 μM sorafenib is synergistic with

https://dx.doi.org/10.1021/acschembio.9b00939
ACS Chem. Biol. XXXX, XXX, XXX−XXX

radiation at both 2 Gy (CDI = 0.65) and 4 Gy (CDI = 0.47), and that this effect is partially suppressible by cotreatment with ferrostatin-1 (Figure S6A). To confirm that the observed synergistic effect between sorafenib and radiation in HT-1080 cells is due to system x_c^- inhibition, we then measured levels of GSH in these cells treated with DMSO or sorafenib and cotreated with 0 or 6 Gy radiation for 24 h. Indeed, significant depletion of GSH was observed in the dual treated sample, when compared to samples treated with DMSO, sorafenib alone, or radiation alone (Figure S6B).

To test the radiosensitizing effects of sorafenib *in vivo*, we treated athymic nude mice implanted with HT-1080 xenograft tumors, as described above, with 40 mg/kg of sorafenib tosylate or vehicle delivered i.p. daily for 14 days, with or without 6 Gy radiation delivered per mouse using SARRP on days 1 and 3. Using two-sample *t* tests, we observed significant differences between the control, radiation-treated, and combination-treated groups (Figure 6C). No difference was observed between the control group and the group treated with sorafenib alone. Two-way ANOVA revealed statistical significance for treatment with sorafenib alone ($p = 0.03$) and radiation alone ($p = 0.006$). Similar to the experiment with IKE, the two factors interacted positively with each other but did not reach significance ($p = 0.18$). No significant differences in weight were observed between any of the groups over the course of the experiment (Figure S5B).

We then sought to confirm that sorafenib inhibits system x_c^- *in vivo*, leading to a depletion of downstream intracellular glutathione. We measured GSH in tumor tissue taken from three randomly selected mice in each group and found significantly lower GSH in tumors treated with either radiation or sorafenib compared to those treated with vehicle. A further significant GSH depletion was observed in dual-treated tumors (Figure 6D).

Analysis of TCGA Data Suggests a Role for *SLC7A11* in Radioresistance of Gliomas. To determine if system x_c^- can potentially be an additional therapeutic target in tumors undergoing radiation therapy, we examined the association between *SLC7A11* expression and methylation and clinical outcomes for all patients diagnosed with glioma in the Cancer Genome Atlas (TCGA) data set.[32,33] Comparing patient groups with low (quartile 1) or high (quartile 4) levels of *SLC7A11* RNA expression, we found that high expression of *SLC7A11* RNA was associated with decreased overall survival (OS) and disease-free survival (DFS, $p < 0.001$). Conversely, *SLC7A11* DNA methylation was associated with improved OS and DFS ($p < 0.001$; Figures 7A, S7). Given that our data suggest that inhibition of system x_c^- sensitizes glioma cells to radiation-induced ferroptosis, we would also expect that RNA expression and DNA methylation of *SLC7A11* is preferentially important for patients treated with radiation over those who are not. In order to further determine whether survival outcomes were specific to radiation therapy, we conducted a subgroup analysis in the data set, in which survival based on gene expression and methylation was stratified by receipt of radiation therapy. For patients who were not treated with radiotherapy, there was no association between survival and levels of *SLC7A11* RNA expression or DNA methylation. However, in patients treated with radiation therapy, high *SLC7A11* RNA expression was associated with decreased DFS ($p < 0.001$), while high DNA methylation was associated with improved DFS ($p < 0.001$; Figure 7B). Taken together, these data support a role for *SLC7A11* in treatment resistance of gliomas toward radiation and suggest a potential benefit for system x_c^- inhibition with IKE or sorafenib during radiation treatment.

IKE Combines with Radiation to Enhance Lipid Peroxidation in *ex Vivo* Slice Cultures of Human Gliomas. To further study the potential of combining small-molecule ferroptosis inducers and radiation for human therapeutic use, we used *ex vivo* samples of human glioma, which were immediately cut from freshly resected tumors and grown as organotypic slice cultures, as previously described.[34] Deidentified patient information for these tumor samples is recorded in Table S4. The slices were then treated with 10 μM IKE, 2 Gy radiation, or a combination of both for 24 h. Then, cells were dissociated and stained with H2DCFDA dye to measure formation of intracellular ROS using flow cytometry. A total of five human samples were tested. Of these, two glioblastomas did not demonstrate an increase in ROS generation following treatment with radiation, whereas three did respond to radiotherapy, including one high-grade oligodendroglioma and two astrocytomas. In the three responsive slice cultures, we also observed a significant enhancement of ROS generation with combination treatment when compared to control (Figure 7C,D). The ROS accumulation was also partially suppressible by cotreating with 10 μM ferrostatin-1, indicating that part of the generated ROS originates from lipid membranes. Tumor cell viability within slices was not assessed, as the number of tumor cells embedded in each slice cannot be normalized between slices. Taken together, these experiments show that certain human gliomas may be susceptible to a combination therapy of a ferroptosis inducer and radiation. However, a mixed response to radiation among all tumors tested suggests that more experiments are needed to better understand which types of glioma might be most sensitive to the proposed treatment regimen.

IKE and Sorafenib Enhance Effects of Radiation to Inhibit Tumor Growth in a Patient-Derived Xenograft of Lung Adenocarcinoma. Finally, we tested the effect of ferroptosis-inducing system x_c^- inhibitors, in combination with radiation, on a patient-derived xenograft (PDX) model of lung adenocarcinoma, a type of cancer commonly treated with radiation therapy. NSG mice engrafted with a human lung adenocarcinoma tumor (TM00219) were evaluated. Intraperitoneal (i.p.) injections of 40 mg/kg of IKE, 40 mg/kg of sorafenib, or vehicle were delivered daily for 14 days, as described above in the HT-1080 xenograft study. On day one of treatment, 0 or 6 Gy radiation was delivered to the tumor site using the SARRP. At the conclusion of the study, we observed significant tumor growth inhibition in the combination-treated group compared to all other groups (Figure 7E,F). In addition, treatment with radiation alone, IKE alone, or sorafenib alone also showed significant tumor control compared to the group treated with vehicle only. This experiment demonstrates the potential applicability of this therapeutic strategy to patients whose cancers currently already receive radiation therapy as a standard of care.

Traditionally, mechanisms of cellular lethality from radiation have focused on the role of clustered DNA damage, in particular double-strand DNA breaks, in the nucleus. This genotoxicity leads to downstream effects such as apoptosis and mitotic catastrophe, which are thought to be the predominant mechanisms of cancer cell death following irradiation.[35] Nevertheless, some prior reports have highlighted the capacity for radiation to produce hydroxyl radicals and even lipid peroxidation in cell membranes.[11,36] With the framework of ferroptosis, a lipid-peroxidation-based form of regulated cell

https://dx.doi.org/10.1021/acschembio.9b00939
ACS Chem. Biol. XXXX, XXX, XXX−XXX

death that can be modulated by a wide arsenal of pharmacological agents and metabolic interventions, it may now be possible to enhance the radiation-induced lipid damage response to kill tumors. This alternative mechanism may be especially effective in tumors with either intrinsic or acquired resistance to the genotoxic effects of radiation, such as those with increased capacity for DNA repair or a defective apoptosis pathway.

Intriguingly, the ferroptosis-inducing molecules erastin and sulfasalazine have been shown previously to potentiate radiation in models of glioma, melanoma, and breast cancer.[37−39] Both of these molecules belong to class I ferroptosis inducers, which inhibit system x_c^- and decreases glutathione synthesis. While these studies noted lowered levels of glutathione to be the cause of the compounds' radiosensitizing effect, the proposed mechanisms of synergy were proposed to be enhanced DNA damage and downstream apoptotic pathways. Our study is the first to link radiation to glutathione depletion resulting in lipid peroxidation and subsequent ferroptotic cell death. These studies together also suggest that altered glutathione metabolism may have the ability to activate distinct cell death mechanisms.

While its ability to deplete glutathione is one likely mechanism by which radiation synergizes with ferroptosis inducers, other possibilities may be considered. γ-rays and X-rays, the most clinically relevant types of radiation therapy, do not damage biological molecules directly, but rather through hydroxyl radical intermediates. Polyunsaturated fatty acids (PUFAs), which are oxidized in ferroptosis, are particularly sensitive to this type of damage given their ability to stabilize a free radical in the bis-allylic position through conjugation and are the most sensitive lipid species to destruction when exposed to high dose radiation.[40] Evidence to support this hypothesis includes reports from two groups that treatment of several cancer cell lines, including astrocytomas and colorectal cancers, with PUFAs results in enhanced cell killing by radiation.[41,42] In addition, in a report identifying the role of ATM in iron metabolism and ferroptosis, the authors speculate that a radiation-induced increase of intracellular iron may be induced through ATM expression and that this increase may provide a further mechanism by which radiation can potentiate ferroptosis.[43] Furthermore, it was recently reported that radiotherapy-activated ATM suppresses SLC7A11, triggering ferroptosis through decreased cysteine uptake and lipid peroxidation.[44] Therefore, it is plausible that one of the ways in which glutathione depletion occurs in our models is due to ATM activation, although the authors agree with our view that many other mechanisms may be involved in this process. Additional studies are required to determine which of these mechanisms are the most relevant in diverse contexts.

While the upstream mechanism by which radiation oxidizes these lipids remains to be elucidated, our lipidomics data suggest that the effects of radiation on lipid species of treated cells as a whole overlap with those produced by a ferroptosis inducer such as IKE. In particular, the profound increase in lysophospholipids, a byproduct of PUFA-phospholipid oxidation, has the potential to serve as a biomarker for ferroptosis induced by both radiation and IKE. For example, the levels of both LysoPI 18:1 and LysoPE 18:1 increased in both groups and showed strong interactions in the combination group, potentially acting as signatures of the synergistic effects between IKE and radiation.

The microbeam results we observed indicate that the interactions between radiation and the ferroptotic pathway occur primarily in the cytoplasm. At the same time, the lower threshold for cell killing by nuclear radiation compared to cytoplasmic radiation suggests that DNA damage is a major cell death modality of radiation. This is potentially because the charged particle radiation used for the microbeam experiments is known to have a higher linear energy transfer (LET), causing more direct DNA damage when compared to γ radiation used in cell culture experiments. Thus, the type of radiation may strongly impact the type of cell death activated, in addition to the tumor context. As ferroptosis inducers are optimized and developed as chemotherapeutic agents, these results suggest that they may be combined with radiation therapy in a variety of contexts, such as when cancers have evolved specific resistance mechanisms to DNA damage and downstream cell death modalities, such as enhanced DNA repair or deficient apoptotic machinery. In particular, the use of this combination therapy in cancers that have undergone EMT is potentially promising, as they have been identified as a resistant state susceptible to GPX4 inhibition and ferroptotic cell death.[45] In these cases, the synergistic effects of this therapeutic strategy may allow lower doses of radiation to be delivered, therefore reducing adverse effects of radiation in healthy tissues.

Finally, using a combination of radiation and IKE or sorafenib, we showed that synergistic tumor cell killing through ferroptosis can be extended to patient-derived models of glioma and lung cancer. Given that these two types of cancer are routinely treated with radiation therapy, our findings potentially pave the way for the first clinical trial focused on ferroptosis as an alternative cell death pathway for tumor control in a therapeutically relevant cancer type.

In summary, we report here that ferroptosis is a mechanism of radiation-induced cancer cell death, and that ferroptosis inducers act as radiosensitizers by potentiating the effects of radiation on cytoplasmic lipid peroxidation leading to cell death, in cell culture, xenograft mouse studies, and patient-derived xenografts and tumor slice cultures. These findings may open up new avenues of treatment for tumors that become resistant to conventional DNA damage and cell death pathways.

■ ASSOCIATED CONTENT

Supporting Information

The Supporting Information is available free of charge at https://pubs.acs.org/doi/10.1021/acschembio.9b00939.

Additional methods and supplemental figures and tables (PDF)

■ AUTHOR INFORMATION

Corresponding Authors

Simon K. Cheng − *Columbia University Irving Medical Center, New York, New York*; Email: sc3225@cumc.columbia.edu

Brent R. Stockwell − *Columbia University, New York, New York, Columbia University Irving Medical Center, New York, New York, and Columbia University, New York, New York*; orcid.org/0000-0002-3532-3868; Email: bstockwell@columbia.edu

Other Authors

Ling F. Ye − *Columbia University, New York, New York*

Kunal R. Chaudhary − *Columbia University Irving Medical Center, New York, New York*

https://dx.doi.org/10.1021/acschembio.9b00939
ACS Chem. Biol. XXXX, XXX, XXX−XXX

Fereshteh Zandkarimi − *Columbia University, New York, New York*
Andrew D. Harken − *Columbia University, Irvington, New York*
Connor J. Kinslow − *Columbia University Irving Medical Center, New York, New York*
Pavan S. Upadhyayula − *Columbia University Irving Medical Center, New York, New York*
Athanassios Dovas − *Columbia University Irving Medical Center, New York, New York*
Dominique M. Higgins − *Columbia University Irving Medical Center, New York, New York*
Hui Tan − *Columbia University, New York, New York*
Yan Zhang − *Columbia University, New York, New York*
Manuela Buonanno − *Columbia University, Irvington, New York*
Tony J. C. Wang − *Columbia University Irving Medical Center, New York, New York*
Tom K. Hei − *Columbia University Irving Medical Center, New York, New York*
Jeffrey N. Bruce − *Columbia University Irving Medical Center, New York, New York*
Peter D. Canoll − *Columbia University Irving Medical Center, New York, New York*

Complete contact information is available at: https://pubs.acs.org/10.1021/acschembio.9b00939

Author Contributions

○Lead contact

Notes

The authors declare the following competing financial interest(s): B.R.S. holds equity in and serves as a consultant to Inzen Therapeutics and is an inventor on patents and applications related to ferroptosis. T.J.C.W. reports personal fees and non-financial support from AbbVie, personal fees from AstraZeneca, personal fees from Cancer Panels, personal fees from Doximity, personal fees and non-financial support from Elekta, personal fees and non-financial support from Merck, personal fees and non-financial support from Novocure, personal fees and non-financial support from RTOG Foundation, personal fees from Wolters Kluwer, outside the submitted work.

■ ACKNOWLEDGMENTS

This work was supported by National Cancer Institute grants R35CA209896 and P01CA087497-17 and National Institute for Neurological Disorders and Stroke grant R61NS109407 to B.R.S., an unrestricted research donation from B. Neustein to S.K.C., and a Louis V. Gerstner, Jr. Scholar Award to S.K.C. These studies used the resources of the Herbert Irving Comprehensive Cancer Center Shared Resources funded in part through Center Grant P30CA013696. The microbeam work was performed at the Radiological Research Accelerator Facility of Columbia University supported by the National Institute of Biomedical Imaging and Bioengineering (NIBIB) grant 5P41EB002033. The small animal radiation research platform was supported by the NIH Biomedical Research Support Shared Instrumentation Grant 1S10OD010631-01A1.

■ REFERENCES

(1) Delaney, G., Jacob, S., Featherstone, C., and Barton, M. (2005) The role of radiotherapy in cancer treatment: estimating optimal utilization from a review of evidence-based clinical guidelines. *Cancer 104*, 1129−1137.
(2) Morgan, M. A., and Lawrence, T. S. (2015) Molecular Pathways: Overcoming Radiation Resistance by Targeting DNA Damage Response Pathways. *Clin. Cancer Res. 21*, 2898−2904.
(3) Souhami, R. L., and Tobias, J. S. (2003) *Cancer and Its Management*, 4th ed., Blackwell Science, Malden, Mass.
(4) Tang, Z., Zeng, Q., Li, Y., Zhang, X., Ma, J., Suto, M. J., Xu, B., and Yi, N. (2017) Development of a radiosensitivity gene signature for patients with soft tissue sarcoma. *Oncotarget 8*, 27428−27439.
(5) Gerszten, P. C., Mendel, E., and Yamada, Y. (2009) Radiotherapy and radiosurgery for metastatic spine disease: what are the options, indications, and outcomes? *Spine (Philadelphia) 34*, S78−92.
(6) Kim, B. M., Hong, Y., Lee, S., Liu, P., Lim, J. H., Lee, Y. H., Lee, T. H., Chang, K. T., and Hong, Y. (2015) Therapeutic Implications for Overcoming Radiation Resistance in Cancer Therapy. *Int. J. Mol. Sci. 16*, 26880−26913.
(7) Willers, H., Azzoli, C. G., Santivasi, W. L., and Xia, F. (2013) Basic mechanisms of therapeutic resistance to radiation and chemotherapy in lung cancer. *Cancer J. 19*, 200−207.
(8) Goldstein, M., and Kastan, M. B. (2015) The DNA damage response: implications for tumor responses to radiation and chemotherapy. *Annu. Rev. Med. 66*, 129−143.
(9) Nehs, M. A., Lin, C. I., Kozono, D. E., Whang, E. E., Cho, N. L., Zhu, K., Moalem, J., Moore, F. D., Jr., and Ruan, D. T. (2011) Necroptosis is a novel mechanism of radiation-induced cell death in anaplastic thyroid and adrenocortical cancers. *Surgery 150*, 1032−1039.
(10) Chaurasia, M., Bhatt, A. N., Das, A., Dwarakanath, B. S., and Sharma, K. (2016) Radiation-induced autophagy: mechanisms and consequences. *Free Radical Res. 50*, 273−290.
(11) Walden, T. L., and Hughes, H. N. (1988) *Prostaglandin and Lipid Metabolism in Radiation Injury*, Springer US, Boston, MA.
(12) Dixon, S. J., Lemberg, K. M., Lamprecht, M. R., Skouta, R., Zaitsev, E. M., Gleason, C. E., Patel, D. N., Bauer, A. J., Cantley, A. M., Yang, W. S., Morrison, B., 3rd, and Stockwell, B. R. (2012) Ferroptosis: an iron-dependent form of nonapoptotic cell death. *Cell 149*, 1060−1072.
(13) Stockwell, B. R., Friedmann Angeli, J. P., Bayir, H., Bush, A. I., Conrad, M., Dixon, S. J., Fulda, S., Gascon, S., Hatzios, S. K., Kagan, V. E., Noel, K., Jiang, X., Linkermann, A., Murphy, M. E., Overholtzer, M., Oyagi, A., Pagnussat, G. C., Park, J., Ran, Q., Rosenfeld, C. S., Salnikow, K., Tang, D., Torti, F. M., Torti, S. V., Toyokuni, S., Woerpel, K. A., and Zhang, D. D. (2017) Ferroptosis: A Regulated Cell Death Nexus Linking Metabolism, Redox Biology, and Disease. *Cell 171*, 273−285.
(14) Yang, W. S., and Stockwell, B. R. (2016) Ferroptosis: Death by Lipid Peroxidation. *Trends Cell Biol. 26*, 165−176.
(15) Yang, W. S., SriRamaratnam, R., Welsch, M. E., Shimada, K., Skouta, R., Viswanathan, V. S., Cheah, J. H., Clemons, P. A., Shamji, A. F., Clish, C. B., Brown, L. M., Girotti, A. W., Cornish, V. W., Schreiber, S. L., and Stockwell, B. R. (2014) Regulation of ferroptotic cancer cell death by GPX4. *Cell 156*, 317−331.
(16) Zhang, Y., Tan, H., Daniels, J. D., Zandkarimi, F., Liu, H., Brown, L. M., Uchida, K., O'Connor, O. A., and Stockwell, B. R. (2019) Imidazole Ketone Erastin Induces Ferroptosis and Slows Tumor Growth in a Mouse Lymphoma Model. *Cell Chem. Biol. 26* (5), 623−633.
(17) Liu, Z., Silke, J., and Hildebrand, J. M. (2018) Methods for Studying TNF-Mediated Necroptosis in Cultured Cells. *Methods Mol. Biol. 1857*, 53−61.
(18) Pikman, Y., Alexe, G., Roti, G., Conway, A. S., Furman, A., Lee, E. S., Place, A. E., Kim, S., Saran, C., Modiste, R., Weinstock, D. M., Harris, M., Kung, A. L., Silverman, L. B., and Stegmaier, K. (2017) Synergistic Drug Combinations with a CDK4/6 Inhibitor in T-cell Acute Lymphoblastic Leukemia. *Clin. Cancer Res. 23*, 1012−1024.

(19) Gao, M., Monian, P., Pan, Q., Zhang, W., Xiang, J., and Jiang, X. (2016) Ferroptosis is an autophagic cell death process. *Cell Res. 26*, 1021−1032.
(20) Gaschler, M. M., Andia, A. A., Liu, H., Csuka, J. M., Hurlocker, B., Vaiana, C. A., Heindel, D. W., Zuckerman, D. S., Bos, P. H., Reznik, E., Ye, L. F., Tyurina, Y. Y., Lin, A. J., Shchepinov, M. S., Chan, A. Y., Peguero-Pereira, E., Fomich, M. A., Daniels, J. D., Bekish, A. V., Shmanai, V. V., Kagan, V. E., Mahal, L. K., Woerpel, K. A., and Stockwell, B. R. (2018) FINO2 initiates ferroptosis through GPX4 inactivation and iron oxidation. *Nat. Chem. Biol. 14*, 507−515.
(21) Dixon, S. J., Patel, D. N., Welsch, M., Skouta, R., Lee, E. D., Hayano, M., Thomas, A. G., Gleason, C. E., Tatonetti, N. P., Slusher, B. S., and Stockwell, B. R. (2014) Pharmacological inhibition of cystine-glutamate exchange induces endoplasmic reticulum stress and ferroptosis. *eLife 3*, No. e02523.
(22) Lomax, M. E., Folkes, L. K., and O'Neill, P. (2013) Biological consequences of radiation-induced DNA damage: relevance to radiotherapy. *Clin Oncol (R Coll Radiol) 25*, 578−585.
(23) Yagoda, N., von Rechenberg, M., Zaganjor, E., Bauer, A. J., Yang, W. S., Fridman, D. J., Wolpaw, A. J., Smukste, I., Peltier, J. M., Boniface, J. J., Smith, R., Lessnick, S. L., Sahasrabudhe, S., and Stockwell, B. R. (2007) RAS-RAF-MEK-dependent oxidative cell death involving voltage-dependent anion channels. *Nature 447*, 865−868.
(24) Colles, S. M., and Chisolm, G. M. (2000) Lysophosphatidylcholine-induced cellular injury in cultured fibroblasts involves oxidative events. *J. Lipid Res. 41*, 1188−1198.
(25) Yang, W. S., Kim, K. J., Gaschler, M. M., Patel, M., Shchepinov, M. S., and Stockwell, B. R. (2016) Peroxidation of polyunsaturated fatty acids by lipoxygenases drives ferroptosis. *Proc. Natl. Acad. Sci. U. S. A. 113*, E4966−4975.
(26) Zou, Y., Palte, M. J., Deik, A. A., Li, H., Eaton, J. K., Wang, W., Tseng, Y. Y., Deasy, R., Kost-Alimova, M., Dancik, V., Leshchiner, E. S., Viswanathan, V. S., Signoretti, S., Choueiri, T. K., Boehm, J. S., Wagner, B. K., Doench, J. G., Clish, C. B., Clemons, P. A., and Schreiber, S. L. (2019) A GPX4-dependent cancer cell state underlies the clear-cell morphology and confers sensitivity to ferroptosis. *Nat. Commun. 10*, 1617.
(27) Randers-Pehrson, G., Johnson, G. W., Marino, S. A., Xu, Y., Dymnikov, A. D., and Brenner, D. J. (2009) The Columbia University Sub-micron Charged Particle Beam. *Nucl. Instrum. Methods Phys. Res., Sect. A 609*, 294−299.
(28) Hei, T. K., Wu, L. J., Liu, S. X., Vannais, D., Waldren, C. A., and Randers-Pehrson, G. (1997) Mutagenic effects of a single and an exact number of alpha particles in mammalian cells. *Proc. Natl. Acad. Sci. U. S. A. 94*, 3765−3770.
(29) Wu, L. J., Randers-Pehrson, G., Xu, A., Waldren, C. A., Geard, C. R., Yu, Z., and Hei, T. K. (1999) Targeted cytoplasmic irradiation with alpha particles induces mutations in mammalian cells. *Proc. Natl. Acad. Sci. U. S. A. 96*, 4959−4964.
(30) Zhou, H., Hong, M., Chai, Y., and Hei, T. K. (2009) Consequences of cytoplasmic irradiation: studies from microbeam. *J. Radiat. Res. 50*, A59−65.
(31) Wu, C. C., Chaudhary, K. R., Na, Y. H., Welch, D., Black, P. J., Sonabend, A. M., Canoll, P., Saenger, Y. M., Wang, T. J. C., Wuu, C. S., Hei, T. K., and Cheng, S. K. (2017) Quality Assessment of Stereotactic Radiosurgery of a Melanoma Brain Metastases Model Using a Mouselike Phantom and the Small Animal Radiation Research Platform. *Int. J. Radiat. Oncol., Biol., Phys. 99*, 191−201.
(32) Brat, D. J., Verhaak, R. G., Aldape, K. D., Yung, W. K., Salama, S. R., Cooper, L. A., Rheinbay, E., Miller, C. R., Vitucci, M., Morozova, O., Robertson, A. G., Noushmehr, H., Laird, P. W., Cherniack, A. D., Akbani, R., Huse, J. T., Ciriello, G., Poisson, L. M., Barnholtz-Sloan, J. S., Berger, M. S., Brennan, C., Colen, R. R., Colman, H., Flanders, A. E., Giannini, C., Grifford, M., Iavarone, A., Jain, R., Joseph, I., Kim, J., Kasaian, K., Mikkelsen, T., Murray, B. A., O'Neill, B. P., Pachter, L., Parsons, D. W., Sougnez, C., Sulman, E. P., Vandenberg, S. R., Van Meir, E. G., von Deimling, A., Zhang, H., Crain, D., Lau, K., Mallery, D., Morris, S., Paulauskis, J., Penny, R., Shelton, T., Sherman, M., Yena, P., Black, A., Bowen, J., Dicostanzo, K., Gastier-Foster, J., Leraas, K. M., Lichtenberg, T. M., Pierson, C. R., Ramirez, N. C., Taylor, C., Weaver, S., Wise, L., Zmuda, E., Davidsen, T., Demchok, J. A., Eley, G., Ferguson, M. L., Hutter, C. M., Mills Shaw, K. R., Ozenberger, B. A., Sheth, M., Sofia, H. J., Tarnuzzer, R., Wang, Z., Yang, L., Zenklusen, J. C., Ayala, B., Baboud, J., Chudamani, S., Jensen, M. A., Liu, J., Pihl, T., Raman, R., Wan, Y., Wu, Y., Ally, A., Auman, J. T., Balasundaram, M., Balu, S., Baylin, S. B., Beroukhim, R., Bootwalla, M. S., Bowlby, R., Bristow, C. A., Brooks, D., Butterfield, Y., Carlsen, R., Carter, S., Chin, L., Chu, A., Chuah, E., Cibulskis, K., Clarke, A., Coetzee, S. G., Dhalla, N., Fennell, T., Fisher, S., Gabriel, S., Getz, G., Gibbs, R., Guin, R., Hadjipanayis, A., Hayes, D. N., Hinoue, T., Hoadley, K., Holt, R. A., Hoyle, A. P., Jefferys, S. R., Jones, S., Jones, C. D., Kucherlapati, R., Lai, P. H., Lander, E., Lee, S., Lichtenstein, L., Ma, Y., Maglinte, D. T., Mahadeshwar, H. S., Marra, M. A., Mayo, M., Meng, S., Meyerson, M. L., Mieczkowski, P. A., Moore, R. A., Mose, L. E., Mungall, A. J., Pantazi, A., Parfenov, M., Park, P. J., Parker, J. S., Perou, C. M., Protopopov, A., Ren, X., Roach, J., Sabedot, T. S., Schein, J., Schumacher, S. E., Seidman, J. G., Seth, S., Shen, H., Simons, J. V., Sipahimalani, P., Soloway, M. G., Song, X., Sun, H., Tabak, B., Tam, A., Tan, D., Tang, J., Thiessen, N., Triche, T., Jr., Van Den Berg, D. J., Veluvolu, U., Waring, S., Weisenberger, D. J., Wilkerson, M. D., Wong, T., Wu, J., Xi, L., Xu, A. W., Yang, L., Zack, T. I., Zhang, J., Aksoy, B. A., Arachchi, H., Benz, C., Bernard, B., Carlin, D., Cho, J., DiCara, D., Frazer, S., Fuller, G. N., Gao, J., Gehlenborg, N., Haussler, D., Heiman, D. I., Iype, L., Jacobsen, A., Ju, Z., Katzman, S., Kim, H., Knijnenburg, T., Kreisberg, R. B., Lawrence, M. S., Lee, W., Leinonen, K., Lin, P., Ling, S., Liu, W., Liu, Y., Liu, Y., Lu, Y., Mills, G., Ng, S., Noble, M. S., Paull, E., Rao, A., Reynolds, S., Saksena, G., Sanborn, Z., Sander, C., Schultz, N., Senbabaoglu, Y., Shen, R., Shmulevich, I., Sinha, R., Stuart, J., Sumer, S. O., Sun, Y., Tasman, N., Taylor, B. S., Voet, D., Weinhold, N., Weinstein, J. N., Yang, D., Yoshihara, K., Zheng, S., Zhang, W., Zou, L., Abel, T., Sadeghi, S., Cohen, M. L., Eschbacher, J., Hattab, E. M., Raghunathan, A., Schniederjan, M. J., Aziz, D., Barnett, G., Barrett, W., Bigner, D. D., Boice, L., Brewer, C., Calatozzolo, C., Campos, B., Carlotti, C. G., Jr., Chan, T. A., Cuppini, L., Curley, E., Cuzzubbo, S., Devine, K., DiMeco, F., Duell, R., Elder, J. B., Fehrenbach, A., Finocchiaro, G., Friedman, W., Fulop, J., Gardner, J., Hermes, B., Herold-Mende, C., Jungk, C., Kendler, A., Lehman, N. L., Lipp, E., Liu, O., Mandt, R., McGraw, M., McLendon, R., McPherson, C., Neder, L., Nguyen, P., Noss, A., Nunziata, R., Ostrom, Q. T., Palmer, C., Perin, A., Pollo, B., Potapov, A., Potapova, O., Rathmell, W. K., Rotin, D., Scarpace, L., Schilero, C., Senecal, K., Shimmel, K., Shurkhay, V., Sifri, S., Singh, R., Sloan, A. E., Smolenski, K., Staugaitis, S. M., Steele, R., Thorne, L., Tirapelli, D. P., Unterberg, A., Vallurupalli, M., Wang, Y., Warnick, R., Williams, F., Wolinsky, Y., Bell, S., Rosenberg, M., Stewart, C., Huang, F., Grimsby, J. L., Radenbaugh, A. J., and Zhang, J. (2015) Comprehensive, Integrative Genomic Analysis of Diffuse Lower-Grade Gliomas. *N. Engl. J. Med. 372*, 2481−2498.
(33) Brennan, C. W., Verhaak, R. G. W., McKenna, A., Campos, B., Noushmehr, H., Salama, S. R., Zheng, S., Chakravarty, D., Sanborn, J. Z., Berman, S. H., Beroukhim, R., Bernard, B., Wu, C.-J., Genovese, G., Shmulevich, I., Barnholtz-Sloan, J., Zou, L., Vegesna, R., Shukla, S. A., Ciriello, G., Yung, W.K., Zhang, W., Sougnez, C., Mikkelsen, T., Aldape, K., Bigner, D. D., Van Meir, E. G., Prados, M., Sloan, A., Black, K. L., Eschbacher, J., Finocchiaro, G., Friedman, W., Andrews, D. W., Guha, A., Iacocca, M., O'Neill, B. P., Foltz, G., Myers, J., Weisenberger, D. J., Penny, R., Kucherlapati, R., Perou, C. M., Hayes, D. N., Gibbs, R., Marra, M., Mills, G. B., Lander, E., Spellman, P., Wilson, R., Sander, C., Weinstein, J., Meyerson, M., Gabriel, S., Laird, P. W., Haussler, D., Getz, G., and Chin, L. (2014) The somatic genomic landscape of glioblastoma. *Cell 157*, 753.
(34) Parker, J. J., Lizarraga, M., Waziri, A., and Foshay, K. M. (2017) A Human Glioblastoma Organotypic Slice Culture Model for Study of Tumor Cell Migration and Patient-specific Effects of Anti-Invasive Drugs. *J. Visualized Exp. 125*, No. e53557.
(35) Eriksson, D., and Stigbrand, T. (2010) Radiation-induced cell death mechanisms. *Tumor Biol. 31*, 363−372.

https://dx.doi.org/10.1021/acschembio.9b00939
ACS Chem. Biol. XXXX, XXX, XXX−XXX

(36) Shadyro, O. I., Yurkova, I. L., and Kisel, M. A. (2002) Radiation-induced peroxidation and fragmentation of lipids in a model membrane. *Int. J. Radiat. Biol. 78*, 211−217.
(37) Sleire, L., Skeie, B. S., Netland, I. A., Forde, H. E., Dodoo, E., Selheim, F., Leiss, L., Heggdal, J. I., Pedersen, P. H., Wang, J., and Enger, P. O. (2015) Drug repurposing: sulfasalazine sensitizes gliomas to gamma knife radiosurgery by blocking cystine uptake through system Xc-, leading to glutathione depletion. *Oncogene 34*, 5951−5959.
(38) Nagane, M., Kanai, E., Shibata, Y., Shimizu, T., Yoshioka, C., Maruo, T., and Yamashita, T. (2018) Sulfasalazine, an inhibitor of the cystine-glutamate antiporter, reduces DNA damage repair and enhances radiosensitivity in murine B16F10 melanoma. *PLoS One 13*, No. e0195151.
(39) Cobler, L., Zhang, H., Suri, P., Park, C., and Timmerman, L. A. (2018) xCT inhibition sensitizes tumors to gamma-radiation via glutathione reduction. *Oncotarget 9*, 32280−32297.
(40) Hammer, C. T., and Wills, E. D. (1979) The effect of ionizing radiation on the fatty acid composition of natural fats and on lipid peroxide formation. *Int. J. Radiat. Biol. Relat. Stud. Phys., Chem. Med. 35*, 323−332.
(41) Vartak, S., Robbins, M. E., and Spector, A. A. (1997) Polyunsaturated fatty acids increase the sensitivity of 36B10 rat astrocytoma cells to radiation-induced cell kill. *Lipids 32*, 283−292.
(42) Cai, F., Sorg, O., Granci, V., Lecumberri, E., Miralbell, R., Dupertuis, Y. M., and Pichard, C. (2014) Interaction of omega-3 polyunsaturated fatty acids with radiation therapy in two different colorectal cancer cell lines. *Clin. Nutr. 33*, 164−170.
(43) Chen, P. H., Wu, J., Ding, C. C., Lin, C. C., Pan, S., Bossa, N., Xu, Y., Yang, W. H., Mathey-Prevot, B., and Chi, J. T. (2019) Kinome screen of ferroptosis reveals a novel role of ATM in regulating iron metabolism, *Cell Death Differ.*, Jul 18. DOI: 10.1038/s41418-019-0393-7.
(44) Lang, X., Green, M. D., Wang, W., Yu, J., Choi, J. E., Jiang, L., Liao, P., Zhou, J., Zhang, Q., Dow, A., Saripalli, A. L., Kryczek, I., Wei, S., Szeliga, W., Vatan, L., Stone, E. M., Georgiou, G., Cieslik, M., Wahl, D. R., Morgan, M. A., Chinnaiyan, A. M., Lawrence, T. S., and Zou, W. (2019) Radiotherapy and immunotherapy promote tumoral lipid oxidation and ferroptosis via synergistic repression of SLC7A11. *Cancer Discovery 9* (12), 1673−1685.
(45) Viswanathan, V. S., Ryan, M. J., Dhruv, H. D., Gill, S., Eichhoff, O. M., Seashore-Ludlow, B., Kaffenberger, S. D., Eaton, J. K., Shimada, K., Aguirre, A. J., Viswanathan, S. R., Chattopadhyay, S., Tamayo, P., Yang, W. S., Rees, M. G., Chen, S., Boskovic, Z. V., Javaid, S., Huang, C., Wu, X., Tseng, Y. Y., Roider, E. M., Gao, D., Cleary, J. M., Wolpin, B. M., Mesirov, J. P., Haber, D. A., Engelman, J. A., Boehm, J. S., Kotz, J. D., Hon, C. S., Chen, Y., Hahn, W. C., Levesque, M. P., Doench, J. G., Berens, M. E., Shamji, A. F., Clemons, P. A., Stockwell, B. R., and Schreiber, S. L. (2017) Dependency of a therapy-resistant state of cancer cells on a lipid peroxidase pathway. *Nature 547*, 453−457.

https://dx.doi.org/10.1021/acschembio.9b00939
ACS Chem. Biol. XXXX, XXX, XXX−XXX

Radiation-Induced Lipid Peroxidation Triggers Ferroptosis and Synergizes with Ferroptosis Inducers

Ling F. Ye[1], Kunal R. Chaudhary[2], Fereshteh Zandkarimi[1], Andrew D. Harken[3], Connor J. Kinslow[2], Pavan S. Upadhyayula[4], Athanassios Dovas[5], Dominique M. Higgins[4], Hui Tan[1], Yan Zhang[1], Manuela Buonanno[3], Tony J. C. Wang[2,6], Tom K. Hei[2,6], Jeffrey N. Bruce[4], Peter D. Canoll[5,6], Simon K. Cheng[2,6,*], Brent R. Stockwell[1,6,7,8,*]

[1]Department of Biological Sciences, Columbia University, New York, NY 10027, USA
[2]Department of Radiation Oncology, Vagelos College of Physicians and Surgeons, Columbia University Irving Medical Center, New York, NY 10032, USA.
[3]Radiological Research Accelerator Facility, Center for Radiological Research, Columbia University, Irvington, NY 10533, USA.
[4]Department of Neurological Surgery, Vagelos College of Physicians and Surgeons, Columbia University Irving Medical Center, New York, NY 10032, USA
[5]Departments of Pathology and Cell Biology, Vagelos College of Physicians and Surgeons, Columbia University Irving Medical Center, 1130 St. Nicholas Ave Rm.1001, New York, NY, 10032, USA.
[6]Herbert Irving Comprehensive Cancer Center, Columbia University Irving Medical Center, New York, NY 10032, USA
[7]Department of Chemistry, Columbia University, New York, NY 10027, USA
[8]Lead contact
*Correspondence: bstockwell@columbia.edu (B.R.S.) and sc3225@cumc.columbia.edu (S.K.C.)

METHODS

RESOURCES

REAGENT	SOURCE	IDENTIFIER
Antibodies		
Anti-phospho histone-H2AX antibody	Millipore	05-636
Fluorescein (FITC) AffiniPure Goat Anti-Mouse IgG (H+L)	Jackson ImmunoResearch	115-095-003
Anti-cleaved caspase 3 antibody	Cell Signaling Technology	9661
Anti-beta actin antibody	Sigma-Aldrich	A5316
Peroxidase AffiniPure Goat Anti-Rabbit IgG (H+L)	Jackson ImmunoResearch	111-035-144
Anti-4 Hydroxynonenal antibody	Abcam	ab46545
Rhodamine Red™-X (RRX) AffiniPure Goat Anti-Rabbit IgG (H+L)	Jackson ImmunoResearch	111-295-144
Anti-dihydropyridine-MDA-lysine adduct mouse mAb 1F83	Reference [1]	N/A
Goat Anti-Mouse IgG H&L (FITC)	Abcam	ab6785
Chemicals, Peptides, and Recombinant Proteins		
Imidazole ketone erastin (IKE)	Reference [2]	N/A
Ras-synthetic lethal 3 (RSL3)	Reference [3]	N/A
Ferrostatin-1 (Fer-1)	Reference [4]	N/A
Deferoxamine	Sigma-Aldrich	D9533
Z-VAD-FMK	Selleck Chemicals	S7023
Necrostatin-1S	Abcam	ab221984
3-Methyladenine	Sigma-Aldrich	M9281
Trolox	Sigma-Aldrich	238813
Staurosporine	Selleck Chemicals	S1421
Doxorubicin	ApexBio	A3966
Rapamycin	PeproTech	5318893
Recombinant human TNFα	ABM	Z100859
Birinapant	BioVision	2597-1
Critical Commercial Assays		
GSH/GSSG Ratio Detection Assay Kit	Abcam	ab13881
TBARS Assay Kit	Cayman	700870
BODIPY 581/591 C11	Thermo Fisher Scientific	D3861
CellTiter-Glo Luminescent Cell Viability Assay	Promega	G7573
RNAeasy extraction kit	QIAGEN	74106
QIAshredder	QIAGEN	79656
High Capacity cDNA Reverse Transcription Kit	Thermo Fisher Scientific	4368814
Power SYBR Green PCR Master Mix	Thermo Fisher Scientific	4368702
Software and Algorithms		
Prism, Version 7.0	GraphPad Software	https://www.graphpad.com/scientific-software/prism/

MassLynx, Version 4.1	Waters	http://www.waters.com/waters/en_US/MassLynx-Mass-Spectrometry-Software-/
XCMS package, Version 3.2.0	Bioconductor	http://packages.renjin.org/package/org.renjin.bioconductor/xcms

CONTACT FOR REAGENT AND RESOURCE SHARING

Further information and requests for resources and reagents should be directed to and will be fulfilled by the Lead Contact Brent R. Stockwell (bstockwell@columbia.edu).

EXPERIMENTAL MODEL AND SUBJECT DETAILS

Cell lines and cell culture information is listed below. The HT-1080 (male), SK-LMS-1 (female), U87 (male), and A549 (male) were obtained from ATCC. PC9 (male) cells were obtained from Sigma-Aldrich. HT-1080 cells were cultured in DMEM with 10% fetal bovine serum, 1% penicillin-streptomycin and 1% non-essential amino acids. SK-LMS-1 cells were cultured in EMEM with 10% fetal bovine serum and 1% penicillin-streptomycin. U87 cells were cultured in in DMEM with 10% fetal bovine serum and 1% penicillin-streptomycin. A549 cells were cultured in DMEM with 10% fetal bovine serum and 1% penicillin-streptomycin. PC9 cells were cultured in RPMI with 10% fetal bovine serum and 1% penicillin-streptomycin. All cells were maintained in a humidified environment at 37°C and 5% CO_2 in an incubator.

The animal models used in the paper is listed below. All animal study protocols were approved by the Columbia University Institutional Animal Care and Use Committee (IACUC). Athymic nude mice (Charles River Laboratories, strain code 490) (male, 8

weeks of age) and NSG mice (The Jackson Laboratory, female, 8 weeks of age) were acclimated after shipping for >3 days before beginning experiments. Mice were fed a standard diet and maintained with no more than 5 mice per cage.

Clonogenic assays

500 cells were seeded per well in 6-well plates in their respective growth media and incubated overnight. The next day, cells were co-treated with DMSO or compounds and radiation using a Gammacell 40 Caesium-137 irradiator (Theratronics). Plates were monitored every day using a light microscope for formation of colonies in the DMSO-treated wells. When colonies of >50 cells are clearly visible, the growth medium was discarded from all plates. The cells were washed with PBS, then fixed and stained with crystal violet solution (0.05% crystal violet, 1% formaldehyde, 1% methanol in PBS). Colonies were then directly visualized and counted.

Cell Titer Glo assay

HT-1080 cells were plated at 1,000 cells per well in white 96-well plates (100 uL per well) in technical duplicates. The cells were then treated with vehicle (DMSO), Ferrostatin-1, DFO, Z-VAD-FMK or Necrostatin-1S and incubated overnight. After 24 h incubation, cells were treated with 0 Gy or 2 Gy radiation using a Gammacell 40 Caesium-137 irradiator (Theratronics) and incubated overnight. After another 24 h, 100 uL of 50% Cell Titer Glo (Promega) 50% cell culture medium was added to each well and incubated at room temperature with shaking for 15 min. Luminescence was

measured using a Victor X5 plate reader (PerkinElmer). Experiments were performed three independent times with different passages for each cell line.

RT-qPCR

RNA was extracted using the Qiashredder and QIAGEN RNeasy Mini kits (QIAGEN) according to the manufacturer's protocol. 2 µg total RNA for each sample was used as input for each reverse transcription reaction. Quantitative PCR reactions were performed using the Power SYBR Green PCR Master Mix (Thermo Fisher Scientific). Triplicate samples per condition were analyzed on an Applied Biosystems 7300 qPCR instrument using absolute quantification settings. Differences in mRNA levels compared to *ACTB* internal reference control were computed between control and experimental conditions using the ΔΔCt method. The primers used in this study are listed below.

ACTB forward: 5'-AGAGCTACGAGCTGCCTGAC-3'

ACTB reverse: 5'-AGCACTGTGTTGGCGTACAG-3'

PTGS2 forward: 5'-ATATGTTCTCCTGCCTACTGGAA-3'

PTGS2 reverse: 5'-GCCCTTCACGTTATTGCAGATG-3'

TBARS assay

2 million cells were seeded in T175 flasks. The next day, cells were treated with compounds and/or radiation to induce MDA formation and incubated overnight. 24 h later, the cells were harvested, counted, and collected at 300 x *g* at 4 °C for 5 min. The cell pellet was resuspended in 100 µl of RIPA buffer and homogenized by pipetting. The

whole lysate was used to determine MDA concentration in each sample. We used the TBARS assay kit (Cayman Chemical) and followed the product instructions.

Lipid ROS assay using flow cytometry

0.5 million cells were seeded in 10 cm dishes. The next day, they were co-treated with ferroptosis-modulating compounds and radiation and returned to the incubator. On the following day, cells were harvested in 15 ml tubes and washed twice with PBS followed by re-suspending in 500 µl of PBS containing 10 µM of BODIPY-C11 dye (Thermo Fisher Scientific, cat# D3861), and incubated at 37 °C for 30 minutes. The cells were then collected at 300 x *g* for 5 minutes, washed with PBS three times, and subjected to the flow cytometry analysis. C6 flow cytometry system (BD Accuri cytometers) was used for the flow cytometer analysis. A minimum of 10,000 cells were analyzed per condition.

Glutathione measurement

1 million cells were seeded on 10 cm dishes. The next day, cells were treated with compounds and/or radiation to induce GSH depletion and incubated overnight. 24 h later, the cells were harvested and counted. Five million live cells from each sample were transferred to new tubes, and centrifuged at 300 x *g* at 4 °C for 5 min. The cell pellet was resuspended in 100 µl of RIPA buffer and homogenized by pipetting. The lysate was centrifuged at 16,700 x *g* at 4 °C for 15 min, and cleared lysate was used to determine the amount of GSH in the sample. We used the GSH/GSSG ratio detection assay kit (Abcam, #ab138881) and followed the product instructions to determine GSH levels.

Immunofluorescence study and quantification of cells

10,000 cells were seeded on cover slips placed inside wells of 6-well plates. The next day, cells were treated with ferroptosis modulators and/or radiation, then returned to the incubator for 30 minutes or 6 hours. After the growth medium was removed, the cells were washed with PBS and fixed with 100 µl 4% paraformaldehyde per well for 10 minutes at room temperature. After three washes with PBS, cells were permeabilized with 100 µl Triton X-100 (0.1% v/v) per well for 10 minutes incubation at room temperature. Non-specific protein binding was blocked with 100 µl of BSA (1% v/v) per well for 20 minutes at room temperature. After removing excess BSA, 100µl of primary mouse monoclonal anti-phospho histone-H2AX antibody (1:500) was added to each well for a 1-hour incubation at room temperature. Cells were washed with PBS and incubated with 100 µl of secondary antibody per well for 45 minutes at room temperature in the dark. Cells were washed with PBS and mounted on slides with one drop of Prolong anti-fade reagent with DAPI (Invitrogen) per coverslip. Slides were stored at 4 °C in the dark before analysis on a Zeiss LSM 700 confocal microscope with constant laser intensity for all analyzed samples.

Comet assay

100,000 HT-1080 cells were seeded per well in 6-well plates and incubated overnight. On the next day, the cells were treated with ferroptosis modulators and/or radiation, then returned to the incubator for 30 minutes or 4 hours before being harvested with trypsin and counted. The comet assay was performed using the CometAssay kit

(Trevigen) following the alkaline comet assay product instructions. All images were captured on a Zeiss LSM 700 confocal microscope with constant laser intensity for all analyzed samples. The fluorescent signal of each comet was analyzed using NIH ImageJ software.

Western blot

1 million cells were seeded in 10 cm dishes and treated with compounds and/or radiation on the next day. After 24 hours, cells were harvested at 300 x *g* at 4 °C for 5 min, resuspended in 50 µl of RIPA buffer and homogenized by pipetting. After quantification by Bradford, samples were mixed with 5X SDS loading buffer and separated by SDS-polyacrylamide gel electrophoresis. After transfer, membranes were blocked for 10 min in Tris-buffered saline (pH 7.4) with 1% Tween-20 (TBS-T) with 5% milk and incubated in primary antibody overnight at 4 °C. Following 3X for 5 min washes in TBS-T, the membrane was incubated with secondary antibodies for 1 hr. The membrane was washed again in TBST 3X for 5 min prior to visualization using enhanced chemiluminescence (ECL Western Blotting Substrate, Pierce). Antibody for cleaved caspase 3 (Cell Signaling Technology, #9661) was used at 1:1000 and detected using a Peroxidase AffiniPure Goat Anti-Rabbit IgG (H+L) (Jackson ImmunoResearch, 111-295-144) at 1:5000 dilution.

Mass spectrometry-based untargeted lipidomics

Sample preparation

Lipids were extracted from each sample as described previously [5]. 5 million cells treated with DMSO or 5 μM IKE for 12 hours, with or without 6 Gy radiation for 24 hours, were scraped and homogenized in 250 mL cold methanol containing 0.01% butylated hydroxyl toluene (BHT) with micro tip sonicator. Homogenized samples were transferred to fresh glass tubes containing 850 mL of cold methyl-tertbutyl ether (MTBE) and vortex-mixed for 30 sec. To enhance extraction efficiency of lipids, the samples were incubated for one hour at 4°C on an orbital shaker. Afterwards, 200 mL of cold water was added to each sample, and incubated for 20 min on ice before centrifugation at 3,000 rpm for 20 min at 4°C. The organic layer was collected followed by drying under a gentle stream of nitrogen gas on ice and stored at -80°C until UPLC-MS analysis. The protein pellet was used to measure protein concentration for normalization using Bio-Rad protein assay. The samples were re-constituted in a solution containing 2-propanol/ acetonitrile/water (4:3:1, v/v/v) containing mixture of internal standard (PLASH® LIPIDOMIX® Mass Spec Standard, Avanti Polar Lipids, INC.) for further UPLC-MS analysis. A quality control (QC) sample was prepared by combining 40 mL of each sample to assess the reproducibility of the features through the runs.

Ultra-high-performance liquid chromatography analysis

Chromatographic separation of extracted lipids was carried out at 55°C on ACQUITY UPLC CSH C18 Column, (130Å, 1.7 μm, 2.1 mm X 100 mm) over a 20-min gradient elution. Mobile phase A consisted of ACN/water (60:40, v/v) and mobile phase B was 2-propanol/ACN/water (85:10:5, v/v/v) both containing 10 mM ammonium acetate and 0.1% acetic acid. After injection, the gradient was held at 40% mobile phase B for 2 min.

At 2.1 min, it reached to 50% B, then increased to 70% B in 12 min. At 12.1 min, changed to 70% B and in 18 min increased to 90% B. The eluent composition returned to the initial condition in 1 min, and the column was re-equilibrated for an additional 1 min before the next injection was conducted. The flow rate was set to 400 mL/min and Injection volumes were 6 μL using the flow through needle mode in both positive and negative ionization modes. The QC sample was injected between the samples and at the end of the run to monitor the performance and the stability of the MS platform. This QC sample was also injected at least 5 times at the beginning of the UPLC/MS run, in order to condition the column.

Mass spectrometry analysis

The Synapt G2 mass spectrometer (Waters, Manchester, U.K.) was operated in both positive and negative electrospray ionization (ESI) modes. For positive mode, a capillary voltage and sampling cone voltage of 3 kV and 32 V were used. The source and desolvation temperature were kept at 120°C and 500°C, respectively. Nitrogen was used as desolvation gas with a flow rate of 900 L/hr. For negative mode, a capillary voltage of -2 kV and a cone voltage of 30 V were used. The source temperature was 120°C, and desolvation gas flow was set to 900 L/hr. Dependent on the ionization mode the protonated molecular ion of leucine encephalin ($[M+H]^+$, m/z 556.2771) or the deprotonated molecular ion ($[M-H]^-$, m/z 554.2615) was used as a lock mass for mass accuracy and reproducibility. Leucine enkephalin was introduced to the lock mass at a concentration of 2 ng/mL (50% ACN containing 0.1% formic acid), and a flow rate of 10 mL/min. The data was collected in duplicates in the centroid data independent (MS^E)

mode over the mass range m/z 50 to 1600 Da with an acquisition time of 0.1 seconds per scan. The QC samples were also acquired in enhanced data independent ion mobility (IMS-MS^E) in both positive and negative modes for enhancing the structural assignment of lipid species. The ESI source settings were the same as described above. The traveling wave velocity was set to 650 m/s and wave height was 40 V. The helium gas flow in the helium cell region of the ion-mobility spectrometry (IMS) cell was set to 180 mL/min to reduce the internal energy of the ions and minimize fragmentation. Nitrogen as the drift gas was held at a flow rate of 90 mL/min in the IMS cell. The low collision energy was set to 4 eV, and high collision energy was ramping from 25 to 65 eV in the transfer region of the T-Wave device to induce fragmentation of mobility-separated precursor ions.

Data pre-processing and statistical analysis

All raw data files were converted to netCDF format using DataBridge tool implemented in MassLynx software (Waters, version 4.1). Then, they were subjected to peak-picking, retention time alignment, and grouping using XCMS package (version 3.2.0) in R (version 3.5.1) environment. For the peak picking, the CentWave algorithm was used with the peak width window of 2-25 s. For peak grouping, bandwidth and m/z-width of 2 s and 0.01 Da were used, respectively. After retention time alignment and filling missing peaks, an output data frame was generated containing the list of time-aligned detected features (m/z and retention time) and the relative signal intensity (area of the chromatographic peak) in each sample. Technical variations such as noise were assessed and removed from extracted features' list based on the ratios of average

relative signal intensities of the blanks to QC samples (blank/QC >1.5). Also, peaks with variations larger than 30% in QCs were eliminated. All the extracted features were normalized to measured protein concentrations measured by BCA assay. Statistical analysis was performed in R (version 3.5.1) environment. Group differences were calculated using two-way ANOVA ($p < 0.05$) and false discovery rate of 1% to control for multiple comparisons.

Structural assignment of identified lipids

Structural elucidation and validation of significant lipid features were initially obtained by searching monoisotopic masses against the available online databases such as METLIN, Lipid MAPS, and HMDB with a mass tolerance of 5 ppm. Fragment ion information obtained by tandem MS (UPLC-HDMSE) was utilized for further structural elucidation of significantly changed lipid species. HDMSE data were processed using MS^E data viewer (Version 1.3, Waters Corp., MA, USA).

Microbeam irradiation and clonogenic assay

The charged particle single cell microbeam at Radiological Research Accelerator Facility (RARAF) at the Center for Radiological Research, Columbia University was used. 300-500 HT-1080 cells were plated on polypropylene film treated with 3.5 μg/cm^2 Cell-Tak adhesive (BD Biosciences). The next day, cells were stained with Hoechst 33342 for 30 min. Cells were imaged, and their center-of-gravity coordinates were registered to automatically locate them by the microbeam control program. For nuclear irradiation, protons ($^1H^+$) were directed by a precision beam to the center of the nucleus.

For cytoplasmic irradiation, protons were directed to two locations 7 μm away from the ends of the major axis of each nucleus, as previously described [6]. In each case, the beam has an accuracy of ±0.2 μm with 95% efficiency. Post-irradiation, cells were trypsinized and re-plated at a density of 500 cells per well in 6-well plates for clonogenic assays.

Immunofluorescence study and quantification of microbeam-irradiated cells

Microbeam-treated cells were washed three times with PBS, fixed for 15 min at room temperature in 4% (w/v) paraformaldehyde in PBS and then washed in PBS. The fixed cells were permeabilized with 0.1% Triton X-100 for 10 min and washed three times with PBS. The cells were incubated for 1 h at room temperature in PBS containing 5% (v/v) goat serum and then incubated for 1 h in the same medium containing Anti-phospho histone-H2AX antibody (Millipore, 05-636, 1:500 dilution) or Anti-4 Hydroxynonenal antibody (Abcam, ab46545, 1:500 dilution). The cells were washed and bound primary antibodies were detected by the reaction with Fluorescein (FITC) AffiniPure Goat Anti-Mouse IgG (H+L) (Jackson ImmunoResearch, 115-095-003, 1:1000 dilution) or Rhodamine Red™-X (RRX) AffiniPure Goat Anti-Rabbit IgG (H+L) Jackson ImmunoResearch, 111-295-144, 1:1000 dilution) for 1 h. Cells were thoroughly washed and the polypropylene layer was cut out and placed on a glass slide. A cover glass was placed on top of the polypropylene layer and mounted using ProLong Diamond antifade mountant with DAPI (ThermoFisher P36962). Samples were examined using a Zeiss LSM 700 confocal microscope with constant laser intensity for all analyzed samples. The intensity above threshold of the fluorescent signal of the bound antibodies was

analyzed using NIH ImageJ software. Fluorescence intensity was obtained using the images generated by Image J software (NIH, Bethesda, MD, USA).

HT-1080 tumor xenograft study in mice

Athymic nude mice (8 weeks; Charles River Laboratories) were injected with four million HT-1080 cells s.c. After ~14 days, when the flank tumors had reached an average volume of approximately 100 cubic millimeters, mice were randomized into 4 groups (vehicle or IKE treatment +/- radiation). 300 µL of vehicle (65% D5W, 30% PEG-400, 5% Tween-80) or 40 mg/kg IKE was delivered i.p. after sterilizing the solutions using a 0.2-micron syringe filter. The injections were repeated daily for 14 days. On days 2 and 4 of vehicle or IKE injections, 0 or 6 Gy radiation was delivered to the tumors using the Small Animal Radiation Research Platform (SARRP). For the sorafenib experiment, the formulation used was 40 mg/kg sorafenib in 5% DMSO, 20% ethanol in water containing 30% w/v cyclodextrin. Other experimental details were identical to the IKE experiment, with the exception that radiation was delivered on days 1 and 3. Tumor size was measured daily using calipers and mouse weight was measured daily. The animal protocols containing all the procedures were approved by Columbia University's IACUC.

Patient-derived xenograft study in mice

Patient-derived xenograft tumor-bearing NSG cohort mice (TM00219, LG1049F Lung, 6-8 weeks of age) were purchased from The Jackson Laboratory. when the flank tumors had reached an average volume of approximately 60 cubic millimeters, mice were

randomized into 4 groups (vehicle or IKE treatment or sorafenib treatment +/- radiation). The experiment was conducted according to the same protocol as the HT-1080 tumor xenograft study, with the exception that a single dose of radiation (sham or 6 Gy) was delivered to the tumor on day 1 of the experiment. The animal protocols containing all the procedures were approved by Columbia University's IACUC.

Immunohistochemistry study and quantification on paraffin-embedded tissue sections

Tumor tissue was fixed in 4% paraformaldehyde (PFA) for 24 h at 4 °C followed by washing three times with PBS. The samples were fixed in paraffin. Six series of 5 mm sections were obtained with a sliding microtome. The serial sections were then mounted on gelatin-coated slide. The paraffin-embedded tissue sections were deparaffinized with xylene three times, 5 min each, followed by rehydrating in 100%, 90%, 70%, and 50% ethanol, two washes 5 min each, then rinsed with distilled water. Antigen retrieval was performed in sodium citrate buffer, pH 6.0, 95-100 °C for 10 min. Sections were then rinsed in PBST, 2 min each. A hydrophobic barrier pen was used to draw a circle on each slide. The slides were permeabilized with PBS/0.4% Triton X-100 twice before non-specific-binding blocking by incubating the sections with 10% goat serum (ThermoFisher 50197Z) for 30 minutes at room temperature. The sections were incubated with mouse anti-MDA mAb 1F83 (1:500 dilution) overnight at 4 °C in humidified chambers. Sections were washed with PBST for twice before incubating with goat anti-mouse IgG H&L (FITC) (Abcam, ab6785, 1:1000 dilution) at room temperature for 1 h. Slides were then washed twice with PBST. ProLong Diamond antifade mountant

with DAPI (ThermoFisher P36962) was added onto slides, which were then covered with the coverslips, sealed by clear fingernail polish and observed under confocal microscopy. All images were captured on a Zeiss LSM 700 confocal microscope with constant laser intensity for all analyzed samples. The intensity above threshold of the fluorescent signal of the bound antibodies was analyzed using NIH ImageJ software.

Quantification and statistical analysis

T-test, one-way ANOVA, and two-way ANOVA were performed in the R environment and GraphPad Prism7 with significance and confidence level 0.05 (95% confidence interval).

METHOD REFERENCES

[1] Yamada, S., Kumazawa, S., Ishii, T., Nakayama, T., Itakura, K., Shibata, N., Kobayashi, M., Sakai, K., Osawa, T., and Uchida, K. (2001) Immunochemical detection of a lipofuscin-like fluorophore derived from malondialdehyde and lysine, *J Lipid Res 42*, 1187-1196.

[2] Larraufie, M. H., Yang, W. S., Jiang, E., Thomas, A. G., Slusher, B. S., and Stockwell, B. R. (2015) Incorporation of metabolically stable ketones into a small molecule probe to increase potency and water solubility, *Bioorg Med Chem Lett 25*, 4787-4792.

[3] Yang, W. S., SriRamaratnam, R., Welsch, M. E., Shimada, K., Skouta, R., Viswanathan, V. S., Cheah, J. H., Clemons, P. A., Shamji, A. F., Clish, C. B., Brown, L. M., Girotti, A. W., Cornish, V. W., Schreiber, S. L., and Stockwell, B. R. (2014) Regulation of ferroptotic cancer cell death by GPX4, *Cell 156*, 317-331.

[4] Skouta, R., Dixon, S. J., Wang, J., Dunn, D. E., Orman, M., Shimada, K., Rosenberg, P. A., Lo, D. C., Weinberg, J. M., Linkermann, A., and Stockwell, B. R. (2014) Ferrostatins inhibit oxidative lipid damage and cell death in diverse disease models, *J Am Chem Soc 136*, 4551-4556.

[5] Zhang, Y., Tan, H., Daniels, J. D., Zandkarimi, F., Liu, H., Brown, L. M., Uchida, K., O'Connor, O. A., and Stockwell, B. R. (2019) Imidazole Ketone Erastin Induces Ferroptosis and Slows Tumor Growth in a Mouse Lymphoma Model, *Cell Chem Biol*.

[6] Wu, L. J., Randers-Pehrson, G., Xu, A., Waldren, C. A., Geard, C. R., Yu, Z., and Hei, T. K. (1999) Targeted cytoplasmic irradiation with alpha particles induces mutations in mammalian cells, *Proc Natl Acad Sci U S A 96*, 4959-4964.

Figure S1. Related for Figure 1.

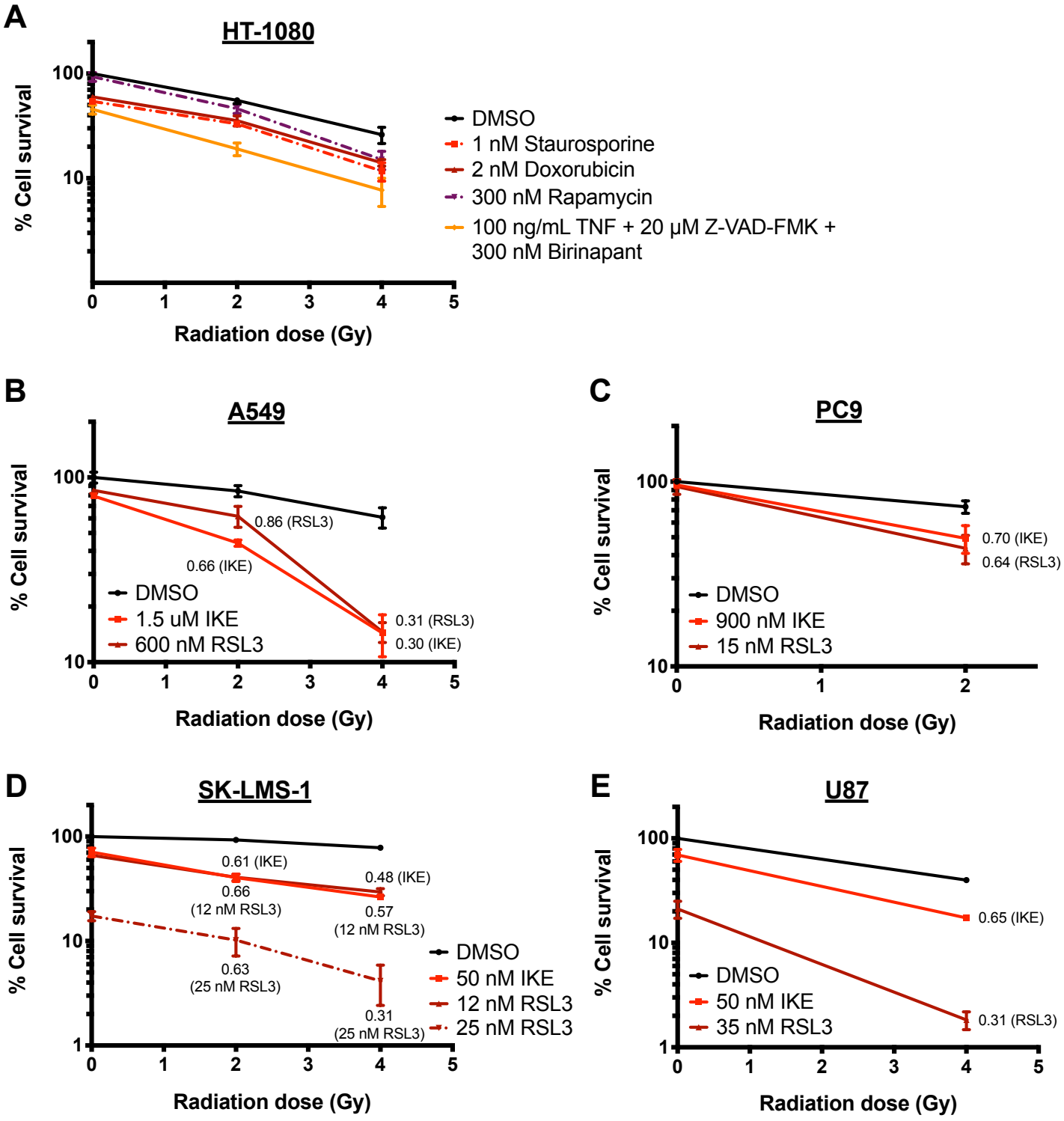

Figure S1. Related to Figure 1 and results section. Survival data of cell lines treated with cell death inducers. A) Dose response of HT-1080 cells treated with DMSO, staurosporine, doxorubicin, rapamycin, or TNFα + Z-VAD-FMK + Birinapant to radiation measured by clonogenic assays. B) to E) Dose response of A549, PC9, SK-LMS-1, and U87 cells treated with DMSO, IKE, or RSL3 to radiation measured by clonogenic assays. CDI values are indicated next to data points according to the formula CDI = AB / (A x B), where AB is the surviving fraction of the combination treatment, and A and B are the surviving fractions of the individual treatments. Data are plotted as mean ± SEM; n = 3 for A) and n = 2 for B) side-by-side replicates. Three biologically independent experiments were performed with similar results.

Figure S2. Related to Figure 2.

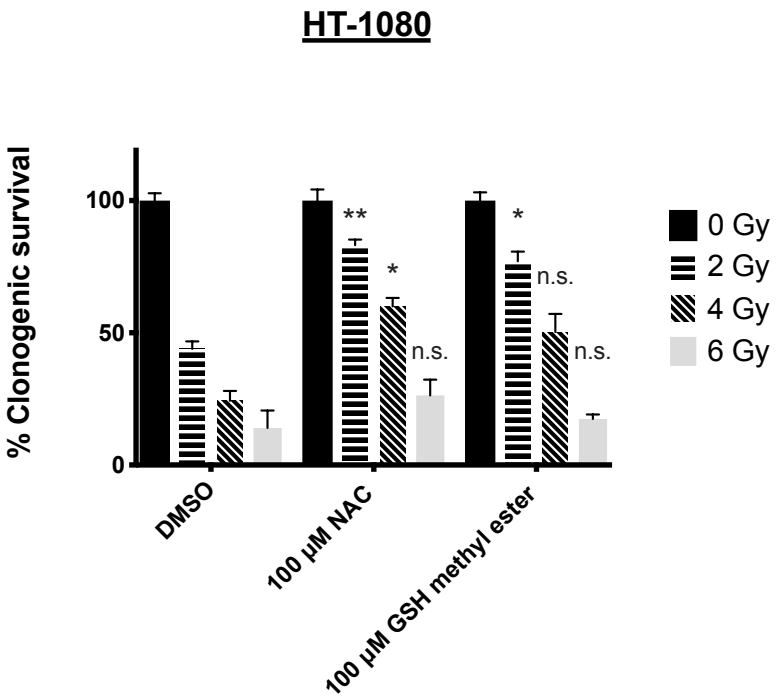

Figure S2. Related to Figure 2 and results section. Clonogenic survival of HT-1080 cells treated with vehicle, N-acetylcysteine, or glutathione methyl ester to 0, 2, 4 and 6 Gy radiation. Data are plotted as mean ± SEM; n = 2 side-by-side replicates. The experiment was repeated twice with similar results.

Figure S3. Related to Figure 3.

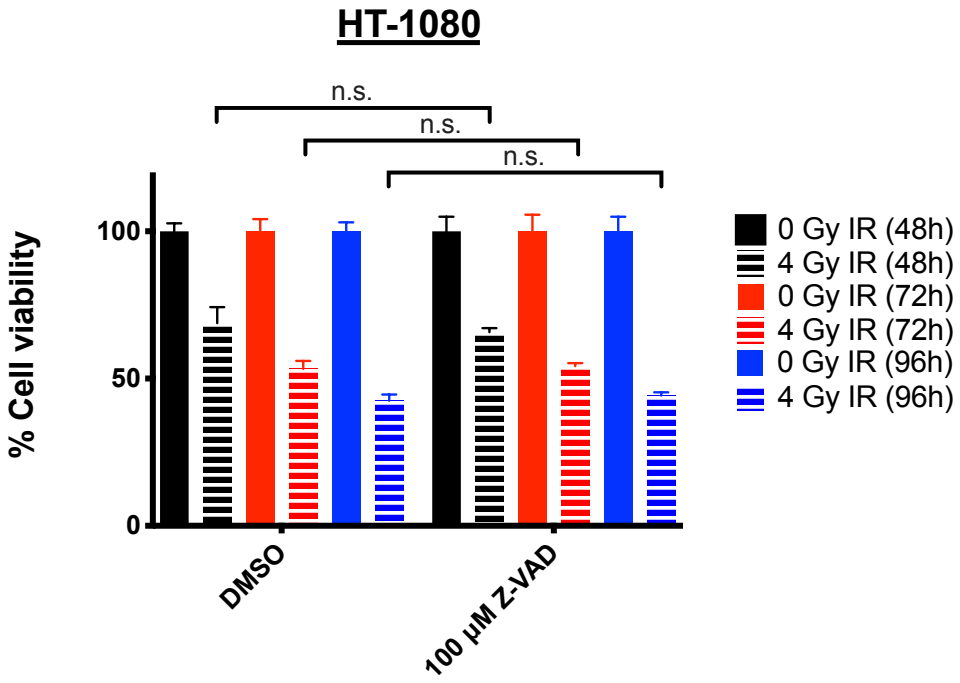

Figure S3. Related to Figure 3 and results section. Cell viability of HT-1080 cells treated with DMSO or Z-VAD-FMK and co-treated with 0 or 4 Gy radiation for 48, 72 or 96 hours measured by Cell Titer Glo. Data normalized to 0 Gy unirradiated controls for each group. Data are plotted as mean ± SEM; n = 3 side-by-side replicates. The experiment was repeated twice with similar results.

Figure S4. Related to Figure 5.

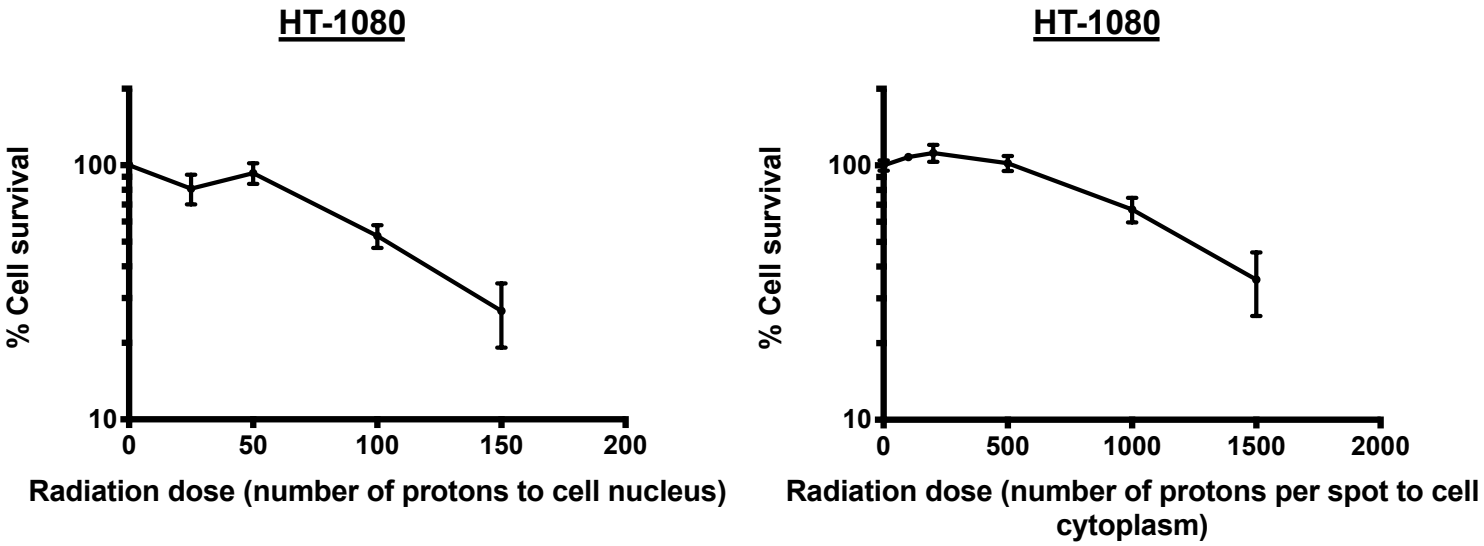

Figure S4. Related to Figure 5 and results section. Dose response of HT-1080 cells treated with nuclear (left) or cytoplasmic (right) microbeam radiation, measured by clonogenic assays. Data are plotted as mean ± SEM; n = 3 side-by-side replicates.

Figure S5. Related to Figure 6.

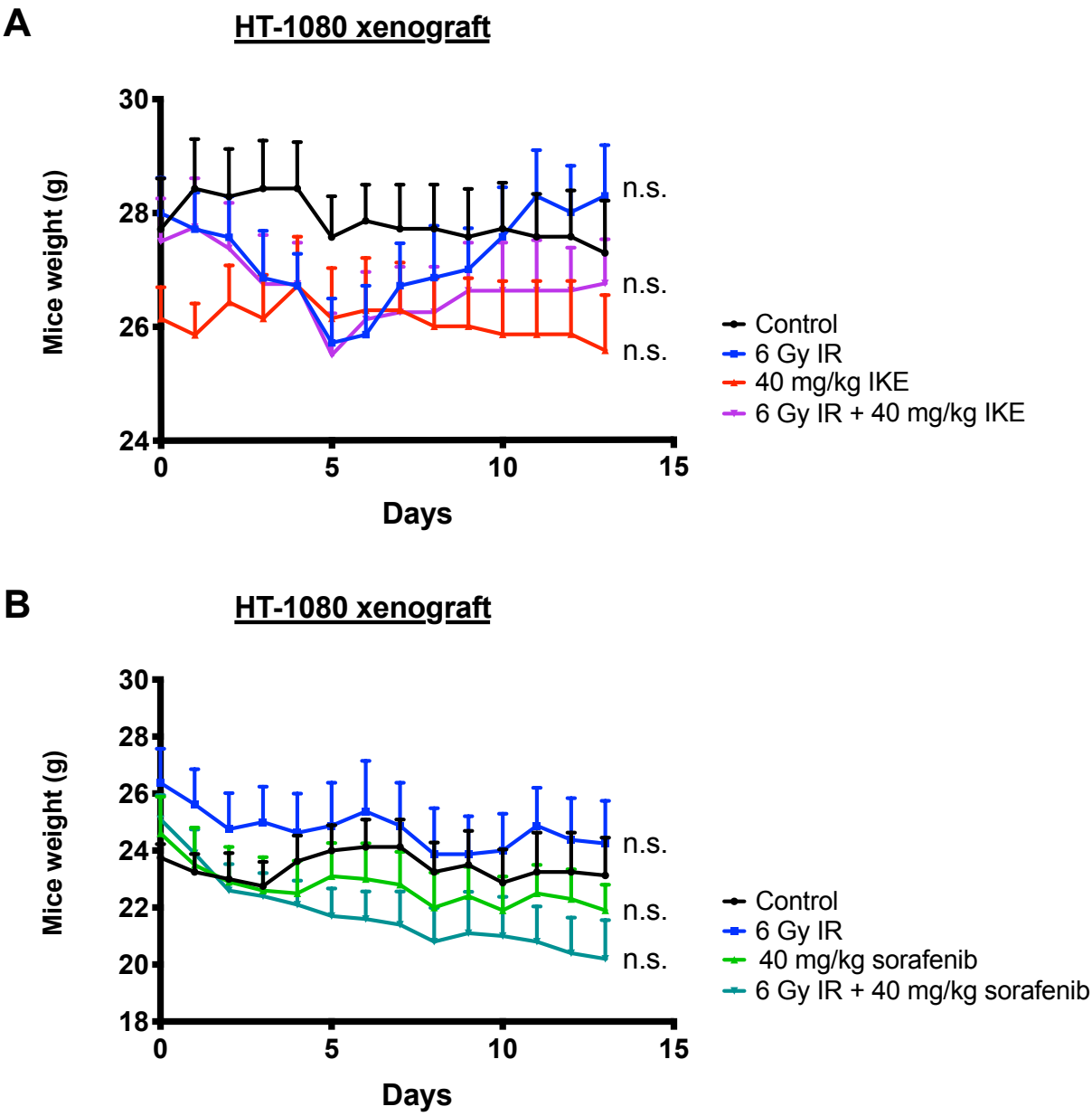

Figure S5. Related to Figure 6 and results section. Mice weight measured by electronic balance over 14 days. Data are plotted as mean ± SEM; n = 7 or 8 mice per group for S5A, n = 4 or 5 mice per group for S5B.

Figure S6. Related to Figure 6.

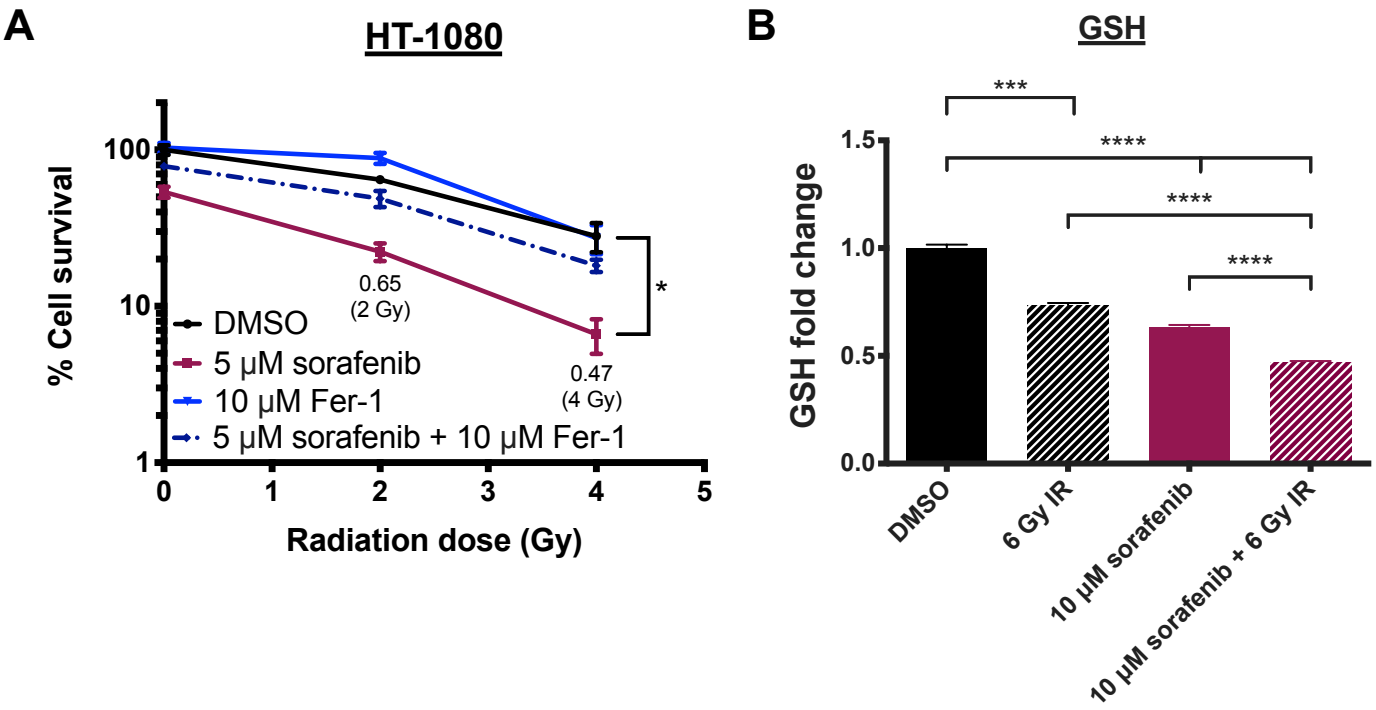

Figure S6. Related to Figure 6 and results section. Effect of sorafenib and radiation on survival and intracellular GSH of HT-1080 cells. A) Dose response of HT-1080 cells treated with DMSO, sorafenib, ferrostatin-1, or sorafenib + ferrostatin-1 to radiation measured by clonogenic assays. CDI values are indicated next to data points according to the formula CDI = AB / (A x B), where AB is the surviving fraction of the combination treatment, and A and B are the surviving fractions of the individual treatments. B) Reduced glutathione (GSH) level detected in HT-1080 cells treated with DMSO or sorafenib and co-treated with 0 or 6 Gy radiation for 24 hours using a fluorometric assay.

**** represents $p<0.0001$, *** represents $p<0.001$, * represents $p<0.05$. Data are plotted as mean ± SEM. n = 3 side-by-side replicates.

Figure S7. Related to Figure 7.

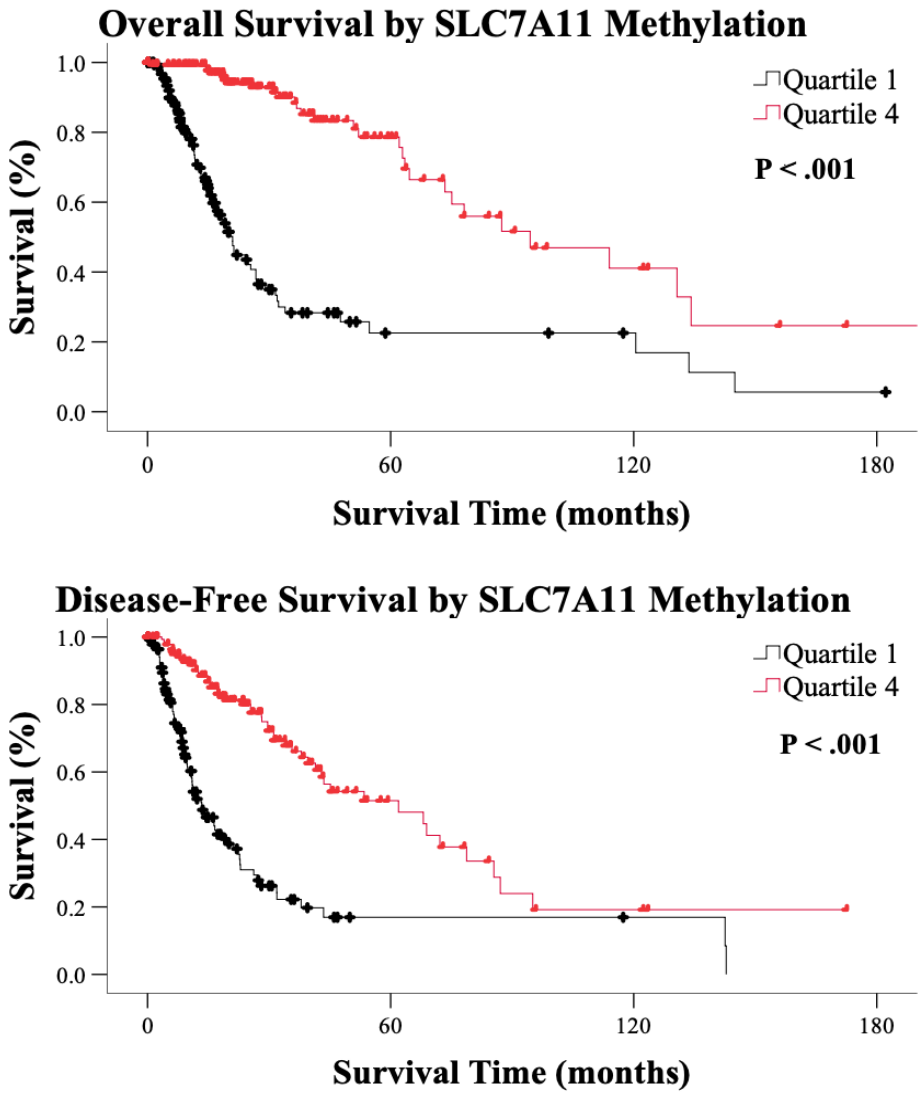

Figure S7. Related to Figure 7 and results section. Kaplan-Meier survival analysis of disease-free survival of TCGA glioma patients in quartile 1 (low) and quartile 4 (high) of SLC7A11 RNA expression (top) or DNA methylation (bottom).

Table S1. Related to Figure 1.

Coefficient of Drug Interaction (CDI) values of cell death inducers in combination with IR in HT-1080 cells. Related to Figure 1 and results section.

Inducer	CDI with 2 Gy IR	CDI with 4 Gy IR
300 nM IKE	0.35	0.17
20 nM RSL3	0.27	0.09
1 nM staurosporine	1.1	0.83
2 nM doxorubicin	1.07	0.9
300 nM rapamycin	0.89	0.62
100 ng/mL TNF + 20 μM Z-VAD-FMK + 300 nM birinapant	0.75	0.65

CDI = AB / (A x B), where AB is the surviving fraction of the combination treatment, and A and B are the surviving fractions of the individual treatments. CDI < 1 indicates synergy, CDI = 1 indicates additivity, and CDI > 1 indicates antagonism.

Table S2. Related to Figure 1.

Highest observed coefficient of Drug Interaction (CDI) values of ferroptosis inducers in combination with IR in HT-1080, SK-LMS-1, U87, A549, and PC9 cells. Related to Figure 1 and results section.

Cell line	IKE + IR	RSL3 + IR
HT-1080	0.17	0.09
SK-LMS-1	0.48	0.31
U87	0.65	0.31
A549	0.30	0.31
PC9	0.70	0.64

CDI = AB / (A x B), where AB is the surviving fraction of the combination treatment, and A and B are the surviving fractions of the individual treatments. CDI < 1 indicates synergy, CDI = 1 indicates additivity, and CDI > 1 indicates antagonism.

Table S3. Related to Figure 4.

List of the annotated lipids that significantly changed among the groups (Two-way ANOVA; FDR-corrected p-value < 0.05), including ionization mode as detected adducts (positive/negative), retention time (RT), m/z values, mass error (∆ppm), molecular formula, and major product ions.

Lipids	Ionization mode	Retention time	m/*z* observed	Mass error (∆PPM)	Molecular formula	Major detected product ions
FA 16:1	$[M-H]^-$	1.99	253.2162	4	$C_{16}H_{30}O_2$	235.2
LysoPE 16:0	$[M-H]^-$	1.42	452.2771	2	$C_{21}H_{44}NO_7P$	255.2
LysoPE 18:0	$[M-H]^-$	2.06	480.3084	2	$C_{23}H_{48}NO_7P$	283.2
LysoPE 18:1	$[M-H]^-$	1.49	478.2925	2	$C_{23}H_{46}NO_7P$	281.2
LysoPE P-16:0	$[M-H]^-$	1.62	436.282	3	$C_{21}H_{44}NO_6P$	418.2
LysoPE P-18:0	$[M-H]^-$	2.39	464.3134	2	$C_{23}H_{48}NO_6P$	446.2
LysoPI 18:1	$[M-H]^-$	1.02	597.3045	0	$C_{27}H_{51}O12P$	281.2/241.2
LysoPC 16:0	$[M+CH_3COO]^-$	1.34	554.3452	2	$C_{24}H_{50}NO_7P$	480.3/255.2
LysoPC 18:0	$[M+CH_3COO]^-$	1.93	582.3767	1	$C_{26}H_{54}NO_7P$	508.3/283.2
LysoPC 18:1	$[M+CH_3COO]^-$	1.42	580.3615	0	$C_{26}H_{52}NO_7P$	506.3/281.2
DAG 16:0_16:0	$[M+H-H_2O]^+$	13.69	551.504	0	$C_{35}H_{68}O_5$	313.3
DAG 16:0_16:1	$[M+H-H_2O]^+$	12.95	549.4883	0	$C_{35}H_{66}O_5$	313.3/311.3
DAG 16:0_18:1	$[M+H-H_2O]^+$	13.74	577.5191	0	$C_{37}H_{70}O_5$	313.3/339.3
DAG 16:1_18:0	$[M+H-H_2O]^+$	14.30	577.5167	4	$C_{37}H_{70}O_5$	341.3
LysoPC 16:0	$[M+H]^+$	1.36	496.3407	1	$C_{24}H_{50}NO_7P$	184.07/(Acyl chain was confirmed in negative mode; 255.2)
LysoPC 18:0	$[M+H]^+$	1.93	524.3717	1	$C_{26}H_{54}NO_7P$	184.07/(Acyl chain was confirmed in negative mode; 283.2)
LysoPC 18:1	$[M+H]^+$	1.42	522.3566	2	$C_{26}H_{52}NO_7P$	184.07/(Acyl chain was confirmed in

						negative mode; 253.2)
LysoPC O-16:0	$[M+H]^+$	1.59	482.3611	1	$C_{24}H_{52}NO6P$	184.07/104.1
LysoPE 18:0	$[M+H]^+$	2.05	482.3247	1	$C_{23}H_{48}NO_7P$	Neutral loss of 141.2/ Acyl chain was confirmed in negative mode; 283.2)
LysoPE 18:1	$[M+H]^+$	1.49	480.3104	4	$C_{23}H_{46}NO_7P$	Neutral loss of 141.2/ Acyl chain was confirmed in negative mode; 281.2)
LysoPE P-16:0	$[M+H]^+$	1.62	438.2983	0	$C_{21}H_{44}NO_6P$	242.2
LysoPE P-18:0	$[M+H]^+$	2.40	466.3296	0	$C_{23}H_{48}NO_6P$	325.2
DAG 16:0_16:0	$[M+Na]^+$	13.69	591.496	0	$C_{35}H_{68}O_5$	313.3
DAG 16:0_16:0	$[M+NH_4]^+$	13.69	586.5407	0	$C_{35}H_{68}O_5$	313.3
DAG 16:0_16:1	$[M+NH_4]^+$	12.95	584.5253	0	$C_{35}H_{66}O_5$	313.3/311.3
DAG 16:0_18:1	$[M+NH_4]^+$	13.73	612.5563	0	$C_{37}H_{70}O_5$	313.3/339.3
DAG 16:1/18:1	$[M+NH_4]^+$	13.34	610.5395	1	$C_{37}H_{68}O_5$	311.3/339.3
DAG 24:0_24:1	$[M+NH_4]^+$	17.40	808.7745	0	$C_{51}H_{98}O_5$	425.4

Table S4. Related to Figure 7.

Characteristics of human gliomas from which organotypic brain slice cultures were derived. Related to Figure 7 and results section.

Tumor bank ID	Age	Sex	Diagnosis
Positive response to radiation			
6163	23	M	Diffuse Astrocytoma, grade II
6177	52	M	Anaplastic Astrocytoma, grade III
6181	32	F	Anaplastic Oligodendroglioma, grade III
Negative response to radiation			
6186	66	M	Glioblastoma, grade IV
6193	67	M	Glioblastoma, grade IV